Revision 3

INTRINSIC CONDITIONS OF MAGMAS FROM THE LUNAR CRATER VOLCANIC FIELD (NEVADA): IMPLICATIONS FOR INTERNAL PLUMBING AND MAGMA ASCENT.

Joaquín A. Cortés[1,2*], Eugene I. Smith[3], Greg A. Valentine[1], Racheal Johnsen[3], Christine Rasoazanamparany[4], Elisabeth Widom[4], Mai Sas[3,5], Dawn Ruth[1].

[1] Department of Geology, 411 Cooke Hall, Buffalo, NY 14260, University at Buffalo, State University of New York, USA.
[2] School of GeoSciences, The University of Edinburgh, Grant Institute, The King's Buildings, West Mains Road, Edinburgh EH9 3JW, UK.
[3] Department of Geoscience, 4505 S. Maryland Parkway, Las Vegas, NV 89154, University of Nevada Las Vegas, USA.
[4] Department of Geology, 114 Shideler Hall, Oxford, OH 45056, Miami University, USA.
[5] Department of Geology, 516 High Street, Bellingham, WA 98225-9080, Western Washington University, USA.

[*]Corresponding Author, caco@buffalo.edu

American Mineralogist, special issue “Volcanic Rocks”

Always consult and cite the final, published document. See http://www.minsocam.org or GeoscienceWorld

ABSTRACT

The northern part of the Lunar Crater Volcanic Field (central Nevada, USA) contains more than one hundred Quaternary basaltic cones and maars and related eruptive products. We focused on four informal units of different ages and locations in the field to test the compositional variability and magma ascent processes within the time span of an individual eruption and the variability between very closely spaced volcanoes with different ages. Based in whole-rock chemistry, mineral chemistry and the calculation of intrinsic properties (pressure, temperature and oxygen fugacity) we found that individual magma batches were generated in the asthenospheric mantle from a heterogeneous garnet lherzolite/olivine websterite source by ~3-5% partial melting. Each magma batch and temporary deep reservoir was a separate entity rather than part of a continuous long-lived reservoir. Magmas ascended relatively fast, stalled and crystallized in the uppermost several kilometres of the mantle near the base of the crust and also stalled at mid-crustal levels with minor or no geochemical interaction with surrounding rocks. Our data also suggest that volcanoes erupting within certain time windows have similar source characteristics and ascent processes whether they are located within a few hundred meters of each other or are separated by many kilometres.

Keywords: Lunar Crater Volcanic Field, monogenetic volcanism, whole-rock chemistry, mineral chemistry, geothermobarometry.

INTRODUCTION

Most of Earth's volcanism occurs at plate boundaries, in association with rifting or subduction, or in high magma-flux intraplate hotspots. However, substantial volcanism also occurs within continents and ocean basins, forming intraplate volcanic fields with relatively low magma fluxes and

Always consult and cite the final, published document. See http://www.minsocam.org or GeoscienceWorld

commonly consisting of small-volume mafic volcanoes with alkaline affinities. Continental intraplate volcanic fields can consist of one to several hundred individual volcanoes, most of which are monogenetic (erupt in a single episode lasting weeks to years), and have lifespans of a few million years (Connor and Conway, 2000). Unlike "hotspot" systems, these fields tend to have a diffuse spatial distribution of eruptive centers and in many cases have no clear migration of eruptive activity with time. Volcanic landforms in intraplate fields are dominated by scoria cones, spatter/agglomerate ramparts, lava fields, maars, and tuff cones, in proportions that depend upon the relative dominance of explosive versus effusive activity and the local hydrologic environment (Valentine and Gregg, 2008; White and Ross, 2011; Brown and Valentine, 2013).

Petrologic studies of intraplate volcanism have tended to focus on "big picture" questions such as the nature of the mantle, or the broad evolution of regional magmatic activity over millions of years; however, recent studies have begun to explore the details of volcanic fields with much higher spatial and temporal resolution, including the complexities often recorded within individual monogenetic volcanoes. An advantage of a study of low magma-volume monogenetic volcanoes is that they may display compositional complexities that are closely related to mantle source characteristics, which may be totally overprinted by crustal reservoir processes in higher volume-flux, long-lived volcanoes. Geochemical and volcanological data from the Plio-Pleistocene Southwest Nevada Volcanic Field in the western U.S.A. for example, suggest that individual volcanoes tap domains of partial melt that are progressively decreasing in volume and degree of partial melting with time (Valentine and Perry, 2007). The domains are inferred to reflect local enrichments in volatile components within the lithospheric mantle source that has been subjected to repeated metasomatic events over ~1 Ga. Valentine and Perry (2006, 2007) suggested that the length scales of the partial melt domains are on the order of kilometers in size and the size of each volcano is proportional to its melt domain size. Brenna et al. (2012) showed how the Jeju Volcanic Field (South Korea) records deepening, increasing degree of melting, and increased melt volumes through time. Detailed studies of individual volcanoes within

Always consult and cite the final, published document. See http://www.minsocam.org or GeoscienceWorld

the Jeju field indicate that each eruption tapped a domain of partial melt on the order of a few kilometers in size and each with a slightly unique composition that may vary within individual eruptions, reflecting mantle heterogeneity (Brenna et al., 2010). The Auckland Volcanic Field (New Zealand) shows similar behavior, with the volumes of individual volcanoes being correlated positively with the degree and spatial scale of partial melting in the asthenospheric source, but with large-volume melt batches interacting more extensively with lithospheric melts compared to smaller batches (McGee et al., 2013). Within the Auckland field, detailed data from the Motukorea volcanic center illustrates complex magma source history even within an individual monogenetic eruption that would commonly be assumed to be a "single batch." Other detailed studies support the perspective that despite their relatively small volumes (typically less than ~1 km^3) and short lives; monogenetic volcanoes are accompanied by relatively complex processes related to magma sources, ascent, and temporary storage (e.g; Paricutín: Rowe et al., 2011; Erlund et al., 2009; Pioli et al., 2008; Luhr and Simkin, 1993; Jorullo: Johnson et al., 2008). Questions remain, however, as to whether the temporal and spatial scales of mantle source domains and the subsequent ascent and eruption of magmas have consistent relationships within and between volcanic fields.

In this work we focus on the products of four monogenetic volcanoes in the Lunar Crater Volcanic Field (central Nevada, USA) to explore two questions. (1) What are the compositional variability and magma ascent processes within the time span of an individual eruption? (2) What is the variability between very closely spaced volcanoes with different ages? Trace element data presented here suggest some degree of small-scale heterogeneity in the asthenospheric mantle, consistent with isotopic data (Rasoazanamparany et al., in review). Thermodynamic calculations of intrinsic variables show that parent melts ascended through two types of magma feeding systems: one in which magma ponded at or just below the base of the crust, and a second where magmas also ponded at mid-crustal levels. The volcanoes were fed by small magma batches that had essentially no chemical interaction with the crust, and ascended rapidly between storage levels and to the surface. In the cases studied,

Always consult and cite the final, published document. See http://www.minsocam.org or GeoscienceWorld

two early eruptions tapped slightly variable mantle source rocks, and the two younger eruptions tapped a different source but one that was relatively homogeneous in space over a length scale of several kilometres and across a time span of several tens of thousands of years. Differences in composition and feeding systems between individual volcanoes seems to be more sensitive to time windows than to spatial variability in the source or crustal plumbing systems.

GEOLOGICAL SETTING AND PREVIOUS WORK

The Lunar Crater Volcanic Field (LCVF) lies at the northern end of a belt of scattered, Plio-Pleistocene basaltic fields that extends north-northeast from Death Valley (California) into central Nevada (Vaniman et al., 1982). The field is in the Basin and Range Province, a broad area of extensional tectonics, but is located centrally within the Province while most other young volcanic fields are found around its edge (e.g., Smith and Leudke, 1984; Brown et al. 2010; Gazel et al., 2012). The LCVF contains more than 100 individual cones with attendant lava fields, and four maars (Valentine et al., 2011; Hintz and Valentine, 2012; Valentine and Cortés, 2013), covering an area of 80 by 20 km extending from the Reveille Range to the Pancake Range (Figure 1).

Previous work in the LCVF has focused on geochemical and petrologic evolution of the field as a whole or of major parts of it, differently from our focus on more local scales (Scott, 1969; Scott and Trask, 1971; Bergman et al., 1981; Bergman, 1982; Lum, 1986; Kargel, 1986); see summary by Foland and Bergman (1992). Several authors used isotopic compositions of LCVF rocks along with samples from many volcanic fields in the western U.S.A. to define regional mantle isotopic domains (Lum et al., 1989; Menzies, 1989; Farmer et al., 1989). In general, isotopic, trace element, and xenolith geothermometry data (Smith, 2000) suggest that the LCVF magmas are sourced in the asthenosphere with characteristics of ocean island basalt (OIB) (Foland and Bergman, 1992), and with evidence of early contamination by crustal rocks (mainly carbonates beneath the early Pliocene Reveille Range

Always consult and cite the final, published document. See http://www.minsocam.org or GeoscienceWorld

volcanoes; Yogodzinski et al., 1996) and by lithospheric mantle (potentially veinlets of intermediate composition in the younger Pancake Range volcanoes; Dickson, 1997).

FIELD DESCRIPTION, STRATIGRAPHY AND PETROGRAPHY

We focus on four different basaltic eruptive units (red area in Figures 1, 2), which are here informally named (from youngest to oldest): Marcath (a.k.a. Black Rock, with cosmogenic exposure age of 38 ± 10 ka; Shepard et al., 1995), Giggle Springs and Mizpah ($^{40}Ar/^{39}Ar$ ages of <81 ± 5 ka and 620-740 ka, respectively; Heizler, 2013) and Hi Desert basalts. Note that we infer the Giggle Springs age to be close to its 81 ka maximum based on the degree of lava surface modification. Field relationships indicate that Hi Desert basalt is older than Giggle Springs, but it is uncertain whether it predates or postdates the Mizpah eruption. The vents for the Giggle Springs, Mizpah, and Hi Desert basalts are located within ~500-600 m of each other, and allow us to assess variations between closely spaced, but different aged, volcanoes as well as potential variations within individual units. The vent for Marcath is ~6 km southeast of these three, allowing to test for variability in magmatic processes that might be related to time rather than co-location.

Hi Desert Basalt (Qhib, age undetermined)

The Hi Desert basalt (Figure 2) crops out as remnants of two small agglomerate cones, 10-20 m high and ~150 m diameter, that are surrounded and partly buried by later lavas and sediments. Hi Desert products are basalts to trachybasalts (Figure 3) notable in the field for the abundant euhedral plagioclase megacrysts, ~1-1.5 cm in size and rarely up to 5 cm. In thin section (neglecting megacrysts), the rock contains ~20% phenocrysts of subhedral olivine (2 and 3 mm in size), 5-10% of

Always consult and cite the final, published document. See http://www.minsocam.org or GeoscienceWorld

phenocrysts of subhedral clinopyroxene (0.5 to 2 mm), and 10% euhedral plagioclase (1 to 2 mm), in a groundmass of plagioclase and ferromagnesian minerals.

Mizpah Basalt (Qmzb; 620-740 ka)

The Mizpah products form an elongate (~2.5 km long, ~800 m wide, 10-15 m thick) lava field with a subdued surface that extends westward from its small, 40 m-high scoria cone source (Figure 2). Mizpah rocks are trachybasalts (Figure 3) and typically porphyritic, containing < 10% subhedral olivine (0.1-0.2 mm) with sparse ~2 mm olivine phenocrysts; 5% subhedral to euhedral clinopyroxene (0.1-0.2 mm); and <10% euhedral plagioclase phenocrysts (0.3-0.6 mm) in some cases with sieve textures. The groundmass has a trachytic texture containing plagioclase and ferromagnesian minerals.

Giggle Springs basalt (Qgsb; <81 ± 5 ka)

Giggle Springs products consist of two tephrite/basanite lava fields (5 km and 1.6 km long, 2-5 m thick; Figures 2, 3) that emanate from the ends of an agglomerate rampart (fissure vent), and partly overlie and partly surround Mizpah lava. The two Giggle Springs lava fields have moderately modified lava surfaces, where rafts of proximal agglomerate are preserved as mounds but areas between mounds have significant accumulations of eolian sediment and desert pavement. Lava levees and a drained lava channel are well preserved within a few hundred meters of the vent area. Megacrysts of olivine and clinopyroxene (up to ~2 cm) and plagioclase (up to ~1 cm) are abundant and ubiquitous in Giggle Springs products. Samples of the lavas contain (neglecting the megacrysts) <5% phenocrysts of subhedral olivine and clinopyroxene (0.1 - 0.2 mm) in an intergranular groundmass of plagioclase and ferromagnesian minerals.

Always consult and cite the final, published document. See http://www.minsocam.org or GeoscienceWorld

Marcath/Black Rock Basalt (Qm; 38 ± 10 ka)

Marcath volcano consists of a ~150 m high, elongate scoria/agglomerate cone with a basal diameter of 900 × 500 m. The cone partly buries a >900 m-long agglomerate rampart that likely records an early fissure-fed phase of the eruption, and is open to the west where aa lavas flowed outward to form two compound lava fields as flows diverted around an older cone onto the adjacent valley floor (Figure 2). The 10-25 m-thick lava fields are 3.2 and 3 km long, and have maximum widths of 1.7 and 1.4 km, respectively. Tephra fall deposits extend south and northeast from the volcano, with thicknesses >4 m near the cone; the northeast lobe can be traced continuously up to 5 km from the vent (Johnson et al., 2014); local patches of ash suggest that it originally extended farther, but wind and water reworking have made it impossible to define the original outer edge of the deposit. The Marcath products are basanites to trachybasalts (Figure 3), ubiquitously containing centimeter-sized megacrysts of plagioclase, olivine, clinopyroxene and amphibole. Under the microscope the samples (neglecting megacrysts) are porphyritic with ~10% of phenocrysts of subhedral olivine (0.1 and 0.2 mm), and ~10% of euhedral (0.1-0.3 mm) plagioclase. The groundmass is microcrystalline with microlites of plagioclase and ferromagnesian minerals.

ANALYTICAL TECHNIQUES

A suite of 24 samples (Table 1) was collected from the four units that are the focus of the study for petrography, whole-rock chemistry, mineral chemistry and geochronology. Samples were also collected for isotopic analyses (Rasoazanamparany et al., in review.). Petrography was determined using the petrographic microscope combined with the study of back-scattered electron images taken with a Hitachi S-4000 scanning electron microscope (SEM) at the University of Buffalo, equipped with

Always consult and cite the final, published document. See http://www.minsocam.org or GeoscienceWorld

an energy dispersive X-ray spectrometer to qualitatively determine the composition of the main mineral phases in the samples.

Whole rock chemistry samples were chipped using a Bico Badger and powdered in a Bico Shatterbox for three minutes. Approximately 20 g of powdered samples were weighed in porcelain crucibles and placed in a furnace at 110 ^{o}C for two hours, cooled and weighed again, and then placed in a 1000 ^{o}C furnace for an additional 1.5 hours in order to measure the loss on ignition. For major-element analyses with x-ray fluorescence spectrometry (XRF), sample powders were mixed with a 50-50 mix of Li-tetraborate and Li-metaborate, melted, and rapidly cooled to form glass disks. The glass disks were ground on 30-micron diamond abrasion pads to expose a fresh and flat analytical surface and then cleaned with isopropanol. Sample powders were prepared for trace element analysis on the XRF by mixing 3 g of binder and 12 g sample powder. Samples were then placed on a Buehler Specimen Mount Press and pressed to pellets. A Panalytical Axios wavelength dispersive XRF was used for both major and trace element analyses at University of Nevada Las Vegas (UNLV). Elements analyzed with the glass fusion disks include SiO_2, Al_2O_3, TiO_2, Fe_2O_3(t), MgO, Na_2O, K_2O, MnO, CaO, and P_2O5, all reported in weight percent. Elements analyzed with the pressed pellets include Sc, V, Ni, Cu, Ga, Rb, Sr, Y, Zr, Nb, Ba, La, Hf, Pb, Th, and U, all reported in parts per million (ppm). The detection limits for most elements is <5 ppm, except La (30 ppm) and Nb (10 ppm).

Rare earth elements were analyzed at Activation Laboratories in Ancaster, Ontario, using a Li-tetraborate-Li-metaborate fusion method on an ICP-MS (see www.actlabs.com for analytical procedure and detection limits)

Main mineral phases were analysed using the JEOL JXA-8900 electron microprobe at UNLV and at the Cornell Center for Materials Research (CMMR) at Cornell University. Conditions of the analysis on both instruments were 15 kV current, a 5-µm beam for ferromagnesian phases, and a 10-µm beam for plagioclase. In the latter, sodium was analysed first in order to avoid loss in the counts of this element. Consistent with hand specimen and petrographic studies, important phenocrysts phases

Always consult and cite the final, published document. See http://www.minsocam.org or GeoscienceWorld

244 are olivine, clinopyroxene, plagioclase and some amphibole, as well as gabbroic and ultramafic
245 enclaves from the Marcath unit. Analyzable glass was not found in the groundmass of the samples.
246 Melt inclusions were not detected in any mineral phases; therefore, calculations of the intrinsic
247 conditions of the different systems are based on the equilibrium between mineral phases, rather than
248 between mineral phases and glass (Putirka, 2008).
249
250 **ANALYTICAL DATA AND RESULTS**
251
252 **Major and Trace Elements**
253
254 Samples from the four volcanoes are tephrites/basanites and basalts to trachybasalts (Table 2,
255 Figure 3) with SiO_2 varying from 43 to 50 wt. %, MgO from 6 to 12 wt. %, and CaO from 8 to 11 wt.
256 %; this range occurs across the four volcanoes as well as within two of the individual volcanoes.
257 Although the Hi Desert basalt seems to be slightly more evolved than the other units, overall no clear
258 trends can be observed in a set of element-versus-MgO variation diagrams (Figure 4).
259 Rare-earth elements compared to OIB basalts strongly suggest an OIB source for the melts
260 (Table 2, Figures 5, 6; Sun and McDonough, 1989). Slight differences in the slope of the REE plots
261 (Figure 5) are well illustrated in a plot of La/Yb vs. Zr/Nb (Figure 7a); Marcath and Giggle Springs
262 units are similar and relatively tightly clustered, while Hi Desert and Mizpah have broader, overlapping
263 fields. Consistent with the main crystallizing phases (olivine, orthopyroxene, clinopyroxene), we have
264 selected Th and Ta as incompatible elements and Cr as compatible (Table 4a) to test for degree of partial
265 melting and further mineral fractionation of these melts. In a plot of Th/Ta vs. Cr/Ta (Figure 7a), no
266 significant differences in the degree of fractionation (Th/Ta) of the source are observed although the
267 figure suggests a variable degree of partial melting (Cr/Ta) in the units (Ta is slightly more incompatible
268 than Th; Tables 4a,b). In a plot of Dy/Yb vs La/Yb (Figure 7b) to test for garnet or spinel in the source,

Always consult and cite the final, published document. See http://www.minsocam.org or GeoscienceWorld

no clear differences in the ratio Dy/Yb are observed (~0.08 to 0.18). Following Barth et al., (2000), we have also plotted the ratio La/Nb vs Nb [ppm] (Figure 8a) and the ratio Nb/Ta vs Nb [ppm] (Figure 8b) to test for crustal contamination. Overall, the samples cluster close to the chondritic ratio although the amount of Nb is several orders of magnitude higher than the sources proposed by Barth et al. (2000).

Mineral Chemistry

Olivine phenocrysts occur in all the units, both as phenocrysts and in the groundmass, and have a range of compositions from Fo_{57} to Fo_{87} for Hi Desert, Fo_{63} and Fo_{87} for Mizpah, Fo_{67} and Fo_{87} for Giggle Springs and for Marcath (Table 3a, Figure 9a), although intermediate-composition olivine is less abundant in Marcath units.

Clinopyroxene phenocrysts and groundmass crystals are generally less common than the olivine phase, but occur in all samples. The main pyroxene phase is diopside in Hi Desert and Mizpah samples, and both diopside and augite (based on the classification of Morimoto, 1989) in Giggle Springs and Marcath. The fact that several of the analyses plot above the diopside limit (Table 3b, Figure 9b) is due to a relatively high Al^{3+} content in their formula, as they contain amounts of the jadeite end-member ($NaAlSi_2O_6$), equivalent to a subtle omphacitic component in clinopyroxenes from Hi Desert, Giggle Springs, and Marcath. This suggests relatively higher-pressure crystallization conditions compared to a normal Ca-Mg-Fe^{2+} clinopyroxene (Morimoto, 1989) and requires the charge balance proposed by Papike et al., (1974) and Cameron and Papike (1981) to estimate iron speciation in the pyroxene formula.

Plagioclase (Table 3c, Figure 9c) has a relatively narrow range of labradoritic compositions in Mizpah, Giggle Springs, and Marcath rocks (An_{61-68}, An_{60-69}, and An_{57-72}, respectively), with a few phenocrysts of an andesine-oligoclase-like phase (~An_{30}). A similar andesine-oligoclase phase was observed in Hi Desert, however plagioclase phenocrysts range in composition between An_{48} and An_{71};

Always consult and cite the final, published document. See http://www.minsocam.org or GeoscienceWorld

a wider range than found in the other three units.

Amphibole was found exclusively in products from Marcath volcano as a phenocryst phase and also as the main phase of <4-cm mafic inclusions that are common around the Marcath edifice and in the proximal areas of Marcath lava flows (Figure 2). Marcath amphibole compositions vary from pargasite to magnesiohastingite and kaersutite (Table 3d, Figure 9d) based on the Leake et al. (1997) cation allocation scheme and classification.

Intrinsic conditions of crystallization

The methods used here to calculate pressure, temperature and oxygen fugacity are based on mineral equilibria of the main crystallizing phases. There are two fundamental aspects considered in these calculations: (1) whether the pairs of mineral phases are in thermodynamic equilibrium (a non-trivial issue in volcanic rocks), and (2) how to determine one value of a given intrinsic condition, based on the calculation of such a value from a data set that is often composed of hundreds microprobe analyses.

Thermometry. Crystallization temperature was estimated using an olivine – clinopyroxene thermometer. There are several formulations of this equilibrium, originally developed by Powell and Powell (1974), all of them based of the interchange of Mg-Fe between olivine and augite:

$$Mg_2SiO_4 + CaFeSi_2O_6 = Fe_2SiO_4 + CaMgSi_2O_6 \quad (1)$$

ol cpx ol cpx

One of its current formulations was proposed by Loucks (1996), wherein the equilibrium constant of Equation (1) depends on temperature through a non-linear relationship that can be solved with a

Always consult and cite the final, published document. See http://www.minsocam.org or GeoscienceWorld

numerical method. In order to assess whether the two mineral phases are in equilibrium we rely on the equilibrium window proposed by Cortés et al. (2005). In their model, since the equilibrium olivine-melt can be equated with the equilibrium clinopyroxene-melt assuming the same melt, the value of the equilibrium constant of the reaction (Equation 1) is constrained if the mineral phases are in equilibrium. According to Cortés et al. (2005) the equilibrium constant, expressed as iron-magnesium ratios, varies between 0.64 and 1.88 with a mean of 1.22. We also rely on the petrography of the samples and assume that equilibrium is attained between two mineral phases in physical contact, although the calculation is not performed on analyses on the interface between the two grains, to avoid Ostwald ripening and elemental diffusion issues between the involved phases.

The composition of each mineral phase in Equation 1, using a large number of analyses, should be normally distributed due to the inherent randomness in crystallization. Because expressing the free energy at equilibrium *implies the calculation of a ratio* between two random variables in which each follow a normal distribution (e.g. the chemical analyses of the mineral phases), the result of the calculation will be a random variable that follows a Cauchy-Lorentz distribution. Since the expected value and variance of a Cauchy-Lorentz distribution are undefined, the best estimation of a measure of central tendency is the median while half the sample interquartile range (HIQR) is a robust estimator of the spread of the statistical sample (e.g. all the calculations performed). The procedure is then used to first calculate all the possible outcomes of temperature for mineral pairs that are assumed in equilibrium, and then to select the median and HIQR of the calculated temperatures. Resulting crystallization temperatures for Hi Desert and Mizpah rocks are between 1050-1100^{o}C, compared to 900-1050^{o}C for the younger Giggle Springs and Marcath units.

Pressure. The lack of glass also precludes crystallization geobarometric calculations based upon melt-mineral phase equilibrium (e.g., clinopyroxene-melt; Putirka, 2008). Nimis and Ulmer

Always consult and cite the final, published document. See http://www.minsocam.org or GeoscienceWorld

(1998) and Nimis (1999) suggest an alternative geobarometer that is based on the structural lattice of clinopyroxene formed in equilibrium with a basaltic melt, such that its composition is not explicitly needed. This geobarometer is relatively insensitive to temperature in alkaline compositions such as those studied here. Because the calculation is performed directly from the composition of clinopyroxene, it is desirable that the distribution of pressures follows a normal distribution if there is one population of clinopyroxene. With this condition, it is straightforward to calculate the mean and standard deviation of the pressure values. Calculated Hi Desert and Mizpah crystallization pressures range between 0.9-1.3 GPa (~30-45 km). The younger units (Giggle Springs and Marcath) have bimodal crystallization pressures with values between 1-1.3 GPa and between 0.3-0.6 GPa (~35-45 km and 10-20 km, respectively).

Empirical observations of amphiboles from calc-alkaline intrusions (Hammarstron and Zen, 1986) show that the amount of total aluminium in amphiboles is proportional to pressure of crystallization (see Ridolfi et al., 2010, for a summary of the different calibrations). Recently, Ridolfi and Renzulli (2012) and Simakin et al. (2012a) have extended the original calibration to mafic products and mafic enclaves, however more work remains to be done in order to have a robust geobarometer based on this mineral phase. The accuracy of the Ridolfi et al. (2010) geobarometer is ± 0.3 GPa (Simakin, pers. comm.) while the Simakin et al., (2012a) model has an accuracy of ± 0.05 GPa. We applied the Ridolfi and Renzulli (2012) model to a set of amphibole phenocrysts found in mafic inclusions within the Marcath lava flow (Table 3d). According to this model, crystallization pressures vary between 0.69-0.75 GPa, overlapping the lower range of values of the clinopyroxene-based crystallization pressures described above. On the other hand, the Simakin et al., (2012a) model did not produce meaningful results in our analyses (negative values), hence we favour the Ridolfi and Renzuli (2012) model, conscious that it is an over-estimation of the pressure with an error of ~25%. The Ridolfi and Renzulli (2012) model also provides temperature estimates between 1037-1070 ^{o}C (consistent with the olivine-clinopyroxene-based crystallization temperatures stated above, taking into account the large

Always consult and cite the final, published document. See http://www.minsocam.org or GeoscienceWorld

error in the calculation), oxygen fugacity between ΔNNO -0.2 and ΔNNO +0.5, and estimated water content in the melt between 5-7 wt%. This range of water content is comparable to those estimated for trachybasalts in the Southwest Nevada Volcanic Field, the nearest Quaternary volcanic field, ~200 km to the south (Nicholis and Rutherford, 2004), and with the higher part of the water content range determined for the Big Pine field, ~250 km west-southwest of LCVF (Gazel et al., 2012).

Oxygen fugacity. Oxygen fugacity estimates are based on the speciation of iron in the clinopyroxene unit formula (Cortés et al., 2006, Simakin et al., 2012b). If the speciation of iron in the clinopyroxene is not known (as it is always the case from a typical electron microprobe analysis), such speciation is calculated based on the charge balance proposed by Papike et al., (1974) and Cameron and Papike (1981). The calculation must also include the contribution of elements such as Na, Ti, Fe^{3+} and Cr, which are not considered in the pyroxene quadrilateral. The intrinsic oxygen fugacity of the system is then estimated assuming equilibrium between the clinopyroxene formula and the melt, although the composition of the melt is not directly needed for the calculation (Cortés et al., 2006). If the temperature is calculated using an independent method, it is possible to additionally determine the absolute oxygen fugacity of the system. As with the barometry described above, one population of clinopyroxene phenocrysts ought to produce values of intrinsic oxygen fugacity that are normally distributed. Cortés et al. (2006) estimated that this approach has a sensitivity of ± 1 QFM unit.

Oxygen fugacity calculations using both Cortés et al. (2006) and Simakin et al. (2012b) methods give comparable values of the oxidation state in the samples. For the older units (Hi Desert and Mizpah) intrinsic oxygen fugacity relative to QFM buffer is estimated between ΔNNO+2 and ΔNNO+4. For the younger magmas (Giggle Springs and Marcath) are relatively reduced with values of intrinsic fugacity between ΔNNO+1 and ΔNNO+2, comparable with amphibole oxygen geobarometry results.

Always consult and cite the final, published document. See http://www.minsocam.org or GeoscienceWorld

Depth of partial melting and origin of the basaltic melts. Depths of partial melting were estimated using two approaches: a silica-melt barometer (Lee et al., 2009), and an orthopyroxene-liquid geobarometer (Putirka, 2008); both calculations are performed using the whole-rock composition of the basaltic products as a proxy of the equilibrium melt. The Lee et al. (2009) technique applies a silica-based barometer that is based solely on the activity of silica in the melt. As a result, it is more reliable and less sensitive to incompatible element variability and mantle composition than earlier barometers (e.g. Wang et al., 2001). The Lee et al. (2009) barometer was calibrated using 433 basalt compositions in equilibrium with olivine and orthopyroxene over a range of temperatures from 1110 to 1800 ˚C and pressures of 1 atmosphere to 7 GPa. Barometer calibration yielded an uncertainty of ± 0.20 GPa (Lee et al., 2009). The thermometer generated is consistent with the barometer and has an uncertainty of ±3% (Lee et al., 2009). When using this barometer, it is critical that the primary magma contains both olivine and pyroxene. Further, the barometer is not calibrated for silica-undersaturated rocks with < 40 wt. % SiO_2, and it is best to choose the most primitive basalt with MgO > 8.0 wt.% for pressure and temperature calculations.

The orthopyroxene-barometer (Putirka, 2008) is calibrated for basalts with SiO_2 contents as low as 35 wt. %, will work for basalt with olivine and both clinopyroxene and orthopyroxene, and is independent of source composition (as long as pyroxene and olivine are in equilibrium with the source at the time of partial melting). Using clinopyroxene + olivine results in almost no increased error relative to olivine + orthopyroxene (Putirka et al., 2012).

Using the method of Lee et al. (2009) in the most primitive whole-rock chemical analyses from our dataset produces temperatures of partial melting of the mantle of the order of 1500-1700^{o}C with pressures between 3-6 GPa, which, for an average density of ~3000 kg/m^3, implies depths of the partial melting between ~100-200 km. The Putirka (2008) calibration indicates that partial melting occurred at temperatures ranging from 1460 to 1650 ^{o}C and pressures between 1.7-3.8 GPa, which implies depths of ~60-130 km, consistent with the depth of the asthenospheric mantle in the region (e.g. Fisher et al.,

Always consult and cite the final, published document. See http://www.minsocam.org or GeoscienceWorld

2010; Kumar et al., 2012).

An important caveat for the Lee et al. (2009) approach is that to apply the model, the source rock is assumed to be a peridotite. In order to assess this condition for the magmas of interest here, we estimate the mineralogy of the mantle sources based on olivine mineralogy (Sobolev et al., 2000). In Figure 10a, we plotted Fe^{2+}/Mn in olivine vs. %Fo, while in Figure 10b we plotted $100xCa/Fe^{2+}$ vs $100xMn/Fe^{2+}$ for the olivine analyses with %Fo > 85, following Sobolev et al. (2007). Based on these plots, we conclude that the most likely source for these magmas has a modal mineralogy that lies between the pyroxenite and peridotite (lherzolite) fields as defined by Sobolev et al. (2007), although nickel content in olivine reported by Sobolev et al., (2007) is higher compared with LCVF olivine. Source identification based on olivine composition is consistent with the approach of Hirschmann (2000) and Petermann and Hirschmann (2003) based on the whole-rock composition, because $FeO/MnO_{(melt)}$ is proportional to the ratio $Fe^{2+}/Mn_{(ol)}$. Thus because the Lee et al. (2009) method assumes a peridotite source, Putirka's (2008) method, which can be applied to a variety of sources as long as they are olivine and pyroxene saturated is favored here.

MELTS modelling. Geothermometry and geobarometry calculations were compared with the MELTS and pMELTS thermodynamic models (Ghiorso and Sack, 1995; Asimow and Ghiorso, 1998; Ghiorso et al., 2002) as a preliminary, but rough validation, since the LCVF conditions are indeed beyond the working limits defined by Ghiorso et al. (2002). We specifically aimed for a preliminary estimation of liquidus temperatures at the calculated pressures by the silica activity barometer, and at the crystallization pressures calculated using the clinopyroxene barometer described above. We also used these thermodynamic models to estimate the potential crystallizing mineralogy to compare with products of the four volcanoes. No calculations of the liquid line of descent were performed because evolved magmas are not present at Lunar Crater. Instead, compositions cluster around SiO_2 ~44-46 wt%.

Always consult and cite the final, published document. See http://www.minsocam.org or GeoscienceWorld

Liquidus temperatures at the pressures of interest were calculated for the most primitive sample of our dataset (sample LC10-20; SiO_2 = 44.02 wt%; Table 5), as well as, for comparison, for a reference pyroxenite sample (Table 2) from the Earth Reference database (http://earthref.org); oxygen fugacity ΔQFM+2 was assumed in both cases in order to constrain the iron speciation in the samples, and 2% of H_2O was assumed in sample LC10-20 consistent with a conservative "wet" liquidus. The temperatures predicted using the Lee et al. (2009) or Putirka (2008) models are comparable to pMELTS-calculated liquidus temperatures (1584°C-1664°C) for both the basalt and pyroxenite given estimated partial melting pressures not higher than 3.8 GPa. The pMELTS model also predicts that the crystallizing phases at 35-45 km depth (equivalent to the crystallization pressures calculated above for Mizpah and Hi Desert, and the deeper of two crystallization pressures that were calculated for Giggle Springs and Marcath) are plagioclase, olivine, clinopyroxene, and orthopyroxene, as well as amphibole and biotite. Except for biotite, all these phases were observed in the volcanic products.

Crystal Size Distribution (CSD)

Crystal size distributions (CSD; Marsh, 1988, 1998; Higgins, 2006) of olivine, clinopyroxene, and plagioclase were measured from back-scattered electron images of samples from the Mizpah, Giggle Spring and Marcath units. Note that olivine CSD was not measured for Marcath products because olivine is rare in these units (Figure 10a). Images were imported into ImageJ freeware (http://rsb.info.nih.gov/ij/) in which long and short axes of the different mineral phases were measured; a total of 200 measurements were performed on each mineral phase in order to have a representative sample of each CSD (Mock and Jerram, 2005; Morgan and Jerram, 2006). Mean crystal aspect ratios were determined using the CSDSlice method (Morgan and Jerram, 2006), fabric was considered massive (e.g. with no foliation), and measurements were not corrected for crystal roundness. All these values as well as the measurements were exported into CSDCorrections 1.4 (Higgins, 2006) in order to

Always consult and cite the final, published document. See http://www.minsocam.org or GeoscienceWorld

calculate the crystal size distribution of each mineral phase. The total slide area, volumetric phase abundance and vesicularity of the samples were determined using built-in features of ImageJ and estimated from the petrography of the samples.

Proximal products of Giggle Springs volcano have smaller sizes than the more distal lava, and there is a partial overlap of the CSDs of the main phenocryst phases although groundmass CSDs are different. The CSD of the olivine phase in Giggle Springs and Mizpah has an inflexion point in the distribution at approximately 0.1 mm for some samples (Figure 11a); olivine phenocrysts in both units have similar distributions except at the smallest sizes. The slope of the CSD of olivine phenocrysts is ~ -16 [mm^{-4}] (r^2 ~ 0.96) and ~ -58 [mm^{-4}] (r^2 ~ 0.95) for groundmass microlites (cut off at 0.1 mm), suggesting residence time of few hours for the phenocrysts using growth rates of 0.2-0.4 mm per day reported for olivines in Hawaiian tholeiites (Maaløe, 2011).

The clinopyroxene CSDs (Figure 11b) are similar between samples from Giggle Springs and Mizpah, but different from Marcath samples, which has consistently larger crystals. The plagioclase CSDs for the different units agree in an intermediate range of sizes between ~0.1 and ~0.3. While this is the upper range for Giggle Springs and Mizpah, it is the lower range for the samples from Marcath (Figure 11c). Oxides (Figure 11d) are substantially different in all the samples (even those from the same unit), suggesting late crystallization events.

DISCUSSION

Melting depths and source composition

Independent of the age and location of the four studied volcanoes, the geochemical data strongly indicate sources located in the asthenosphere, at depths between 60 and 130 km based on the Putirka (2008) orthopyroxene barometer. Considering Fe^{2+}/Mn and Ca/Mg in olivine phenocrysts with %Fo > 85, the source material is likely to have a modal mineralogy between pyroxenite and peridotite (Petermann and Hirschmann, 2003; Tuff et al., 2005; Sobolev et al., 2007; Herzberg, 2011). The most

Always consult and cite the final, published document. See http://www.minsocam.org or GeoscienceWorld

493 likely source is an olivine websterite, although the nickel content in the LCVF olivine is lower (less
494 than 2000 ppm) than the reported values by Sobolev et al., (2007) for pyroxenite or peridotite (between
495 2000 and 4000 ppm). The lower concentration of nickel in olivine suggests a low-Ni source (Herzberg,
496 et al., 2013), although Ni content in whole-rock analyses is within reasonable values (120 to 330 ppm).
497 A possible explanation for this difference might be related to the oxidation state of the magmas.
498 Oxidation state of the depleted and enriched mantle is thought to be close to QFM and NNO+1
499 respectively (Balhaus, 1993). Our estimation of the oxygen fugacity by the clinopyroxene and
500 amphibole formulas seems to indicate more oxidizing conditions for these basalts thus implying
501 changes in oxygen fugacity during ascent and the main crystallization event. The more oxidizing
502 conditions might have affected Ni^{3+} concentrations in the basaltic melt, a species that cannot enter in
503 the olivine formula due to its charge, although the specific relation of the oxygen fugacity and the
504 speciation of nickel is not yet completely understood. A plausible explanation for the more oxidizing
505 conditions during crystallization is likely to be related to the water content of these magmas. The
506 presence of amphibole seems to indicate a relatively high amount of water, which, depending on its
507 speciation, has been linked to changes in the oxidation state of melts (e.g. Barker and Rutherford,
508 1996).

509 Rare-earth element ratios are helpful for estimating the depth of partial melting as well as the
510 mineralogy and chemistry of the source, because of the different solid/melt distributions of REE in
511 spinel vs. garnet bearing peridotite/pyroxenite. Heavy rare-earth elements like Yb are highly
512 compatible in garnet while light-rare earth elements like La are incompatible; therefore partial melting
513 of peridotite or pyroxenite containing garnet will produce melts with high La/Yb. Variable degrees of
514 partial melting will result in changes in La/Yb such that the higher degree of melting, the lower La/Yb.
515 Further, middle-rare earth element (MREE)-heavy rare earth element (HREE) ratios are sensitive to
516 whether garnet exists as a residual phase in the source, because HREEs like Yb are retained by garnet
517 during a melting event. This produces large changes in MREE/HREE in magmas generated by melting

Always consult and cite the final, published document. See http://www.minsocam.org or GeoscienceWorld

518 of a garnet-bearing source, a change that is especially prominent with larger degrees of partial melting.
519 Garnet is a relatively refractory mineral and does not significantly contribute to the melt phase until
520 larger degrees of melting. At small melt fractions, melting of olivine or pyroxene results in little to no
521 change in in MREE/HREE (Dy/Tb) because of similar partition coefficients for Dy and Tb in olivine
522 and pyroxene (e.g., D_oDy/D_oYb=0.75 to 1.5 for clinopyroxene; Chazot et al, 1996). This results in
523 melting trajectories that are relatively flat (or with slightly decreasing Dy/Yb) until about 30% melting.
524 For higher degrees of melting, Dy/Yb decreases rapidly as garnet is melted. In the case of the Lunar
525 Crater volcanoes La/Yb varies from 3 to 15 with the higher ratios suggesting a garnet source (Figures
526 7a,c, 12a,b). The mode of a typical garnet lherzolite is 60% olivine, 20% orthopyroxene, 8%
527 clinopyroxene and 12% garnet (Thirwall et al, 1994). This source produces melts that are too high in
528 Dy/Yb to match Lunar Crater magmas (Figure 12a). If, however, garnet is not as abundant in the
529 source (5 to 8%), modelled melts provide a much better match to the sample set. We also modelled the
530 melting of a spinel lherzolite with 57.8% olivine, 27% orthopyroxene, 11.9% clinopyroxene and 3.3%
531 spinel. Although this source produced melts with relatively constant Dy/Yb, the value of the ratio was
532 much to low to match the dataset. Based on Figure 10b and following Sobolev et al., (2007), we have
533 also modelled the source as an olivine websterite (i.e. a composition between lherzolite and pyroxenite)
534 with 30-35% olivine, 30-40% orthopyroxene, 20-30% clinopyroxene, and 5-11% garnet (Table 4b).
535 Results using this source are similar to the lherzolite models (Figure 12b) except that the final melt has
536 a lower Dy/Yb. Our conclusion is that the source of Lunar Crater magma has a composition between a
537 garnet lherzolite and an olivine websterite containing 5 to 8% garnet. Consistency between this result
538 and that of the independent method based upon olivine Fe^{2+}/Mn and 100xCa/Mg ratios reinforces this
539 interpretation. Note that we did not calculate major element models involving partial melting because
540 of the sensitivity of melt chemistry to source composition. Meaningful major element models would
541 require knowledge of major element chemistry of the source. This information is at present not known
542 well enough for Lunar Crater.

Always consult and cite the final, published document. See http://www.minsocam.org or GeoscienceWorld

543

544 ***Magma evolution***

545 The variation of Th/Ta is used here to determine the degree of fractionation because both
546 elements are incompatible, however Ta is more incompatible than Th (Table 4b) while Cr/Ta varies
547 with different degrees of partial melting in a source containing an olivine websterite component (Cr is
548 highly compatible in both ortho- and clinopyroxene). The narrow range of Th/Ta values relative to
549 Cr/Ta (Figure 7b) indicates variable differences in the degree of partial melting within units, while the
550 trace element variability (e.g., Figure 6) is consistent with small variations in source composition. On
551 the other hand, there is little evidence for systematic fractionation processes in the resulting magma
552 batches as evidenced by nearly constant Th/Ta ratios (Figure 7b).

553 In order to generate the basaltic compositions similar to those reported in Table 2, the required
554 amount of partial melting of a olivine websterite/lherzolite source is ~3-5% based on the batch model
555 calculations presented in Figures 12a,b.

556

557 ***Source Heterogeneity***

558 Source heterogeneity is evident between different, but closely spaced, volcanoes (e.g., Giggle
559 Springs compared to Hi Desert; Figure 7a) and within individual volcanoes (e.g., Mizpah, and possibly
560 Hi Desert). The spatial scale of subtle mantle variability must be similar to the scale of the partial melt
561 domains tapped by the older Hi Desert and Mizpah feeding systems. These observations suggest lateral
562 length scales of ~500 m or less for compositional heterogeneity in the source, if the magmas were
563 sourced at similar depths. In contrast, the two younger volcanoes (Giggle Springs and Marcath) had
564 essentially identical sources based upon the data presented here, even though the volcanoes are ~6 km
565 apart and have age differences of several tens of thousands of years; furthermore, their sources were
566 homogeneous on the scale of the individually tapped melt domains. We realize that melts can travel
567 laterally from source to surface, implying that in some cases, source areas may not lie directly below

Always consult and cite the final, published document. See http://www.minsocam.org or GeoscienceWorld

vents. If this is the case for the northern Lunar Crater volcanoes, our stated spatial scale of source heterogeneity should be regarded as a minimum estimate. Figures 8a,b suggest that although the samples are close to chondritic Nb/Ta and La/Nb, Nb [ppm] is several order of magnitude higher than the mantle or the upper crust and is especially enriched in the younger units (up to 90 ppm in Marcath). This result strongly suggests the addition of an additional crustal (oceanic) component. Isotopic data (Sr Nd Pb, Hf and Os) also indicate a heterogeneous source over very small spatial scales, likely related to ancient subduction processes and consistent with our interpretation (Rasoazanamparany et al. in review).

Magma Ascent and lithospheric contamination

Crystallization occurred at depths of 30-45 km beneath the four volcanoes, with additional crystallization at 10-20 km for the two younger units. Crustal thickness in the area is estimated at 30-35 km (Gilbert and Sheehan, 2004). Thus, enriched melts generated in the asthenospheric mantle travelled relatively unimpeded to near or just beneath the base of the crust, where all four magma batches ponded and underwent up to 50% crystallization as determined from MELTS modelling. The intrinsic variables and the lack of evidence for crustal contamination (Rasoazanamparany et al., in review) indicate that magmas feeding the two older volcanoes, Mizpah and Giggle Springs, ascended rapidly from near the base of the crust to the surface without intermediate ponding.

In contrast, the younger Giggle Springs and Marcath magmas apparently stalled at mid-crustal depths and underwent further crystallization. Fundamental differences in the CSD of their main mineral phases suggest that their mid-crustal reservoirs were not connected to each other, which is also consistent with the likely age difference between the two (38±10 ka and 81±5 ka for Marcath and Giggle Springs, ~620-740 ka for Mizpah). Amphibole crystallized in Marcath's crustal reservoir, and is present in the eruptive products as megacrysts. This phase has only been observed at Marcath, implying either that: (1) there was a slight difference between the crystallization conditions of Marcath and

Always consult and cite the final, published document. See http://www.minsocam.org or GeoscienceWorld

Giggle Springs such as higher water content in the former, while pressure, temperature and oxygen fugacity were similar; or (2) that the amphibole efficiently separated from or was completely assimilated by the soon-to-be-erupted Giggle Springs magma. Arguing against complete assimilation is the observation that resorption of >1 cm amphiboles during the short time scale of final ascent might not be feasible. Mafic enclaves at both Marcath and Giggle Springs volcanoes likely represent crystallization products of these or other ponded magma batches that had not yet solidified; in the latter case, temporary stalling allowed for thermal and chemical interactions that facilitated entrainment of the enclaves (e.g., Valentine and Hirano, 2010).

Despite the mid-crustal ponding of Giggle Springs and Marcath magmas, the lack of evidence of crustal contamination (supported both by the major and trace element chemistry, and by isotopic data; Rasoazanamparany et al., in review) indicates that ascent between storage levels, and between the crustal reservoir and the surface, was rapid. Rapid ascent is a common feature of intraplate, small volume alkali-basalt volcanoes (e.g., Luhr et al., 1995; Valentine and Perry, 2007; Smith et al., 2008; Muffler et al., 2011). The lack of contamination, even though the magma did pond in the mid-crust, is consistent with the volcanoes being fed by small, single batches of magma. When a small batch of magma ponds it is expected that the margins will rapidly chill, increasing in local viscosity and potentially solidifying. This isolates of the inner part of the intrusion from country rocks both chemically and mechanically, until crystallization causes the volatile content to increase sufficiently in the melt to drive dike propagation and final magma ascent to the surface. In contrast, relatively large and repeated magma batches might convect vigorously and retard development of a thick chilled margin and provide enough heat to partly melt and assimilate wall rocks.

An alternative explanation of the deeper-derived phenocrysts is that the Giggle Springs and Marcath magmas did not stall at the deeper 30-45 km level, but simply entrained crystals from that depth that had formed during ponding of earlier (e.g., Mizpah, Hi Desert) magmas. We view this as unlikely because if younger magmas were entraining material as they migrated upwards we would

Always consult and cite the final, published document. See http://www.minsocam.org or GeoscienceWorld

expect them to sample a variety of upper mantle and crustal rocks, not just the products of earlier magma batches.

The final stage on the evolution of these volcanic products is eruption after the ponded magmas have crystallized olivine, clinopyroxene, plagioclase and traces of amphibole. The composition of the amphibole crystals (kaersutite to pargasite/magnesiohastingite) and its stability suggest that this phase is derived either from a metasomatized lithospheric mantle or crystallized from an alkaline melt derived from a peridotite + olivine websterite source (Mayer et al., 2014). Our data are consistent with the latter, phenocrystic origin, for this phase.

The CSDs of one the younger volcanic products (Giggle Springs lava) suggest short crustal residence time, and the further crystallization and growth of olivine, clinopyroxene and an oxide phase, during eruption. Most of the samples have well developed groundmasses rather than glassy matrixes, indicating that subsolidus temperatures were reached slowly after the lava was emplaced in its final location.

IMPLICATIONS

The original motivation for this study was to address two questions: (1) *what are the compositional variability and magma ascent processes within the time span of an individual eruption?* The results presented here indicate two main behaviors of the four studied volcanoes. Individual magma batches were fed by slightly heterogeneous source material for the two older volcanoes, but the younger of the two volcanoes' source rocks were relatively homogeneous even over distances of several kilometres and time differences of tens of thousands of years. Each magma batch stalled and crystallized in the uppermost several kilometres of the mantle near the base of the crust. Even for the closely spaced volcanoes (Mizpah, Hi Desert, and Giggle Springs), the age differences of 10s to 100s

Always consult and cite the final, published document. See http://www.minsocam.org or GeoscienceWorld

643 ka and lack of substantial fractionation suggest that each magma batch and temporary deep reservoir
644 was a separate entity rather than part of a continuous long-lived reservoir. Magmas feeding the
645 Marcath and Giggle Springs volcanoes also stalled at mid-crustal levels. From the evidence at hand it
646 appears that ascent rates from source to storage levels, and from final storage to eruption, were relative
647 rapid with no geochemical interaction with surrounding rocks. (2) *What is the variability between very*
648 *closely spaced volcanoes with different ages?* The Mizpah and Hi Desert magmas have subtle
649 compositional variability, but time is a major factor as well. Volcanoes erupted within certain time
650 windows (an older time window for Mizpah and Hi Desert, and a younger 0-100 ka window for Giggle
651 Springs and Marcath) have similar source characteristics and ascent processes whether they are located
652 within a few hundred meters of each other or are separated by many kilometres. If each monogenetic
653 volcano is fed by a single small-volume batch of magma, with source and feeder system length scales
654 on the order of hundreds of meters to a few kilometres (e.g., Valentine and Perry, 2006, 2007; Valentine
655 and Keating, 2007; Brenna et al., 2012), it is not clear why volcanoes that are several kilometres and
656 tens of thousands of years apart would have such similar magma dynamics. Preliminary data from
657 other parts of the Lunar Crater Volcanic Field are suggesting that this time window-dependent behavior
658 might be general over larger distances; testing this and developing a field-scale conceptual model are
659 topics of current research.
660
661
662 **ACKNOWLEDGEMENTS**

663 The authors acknowledge the editorial management of Thomas Shea and the reviews of Alexander
664 Simakin, Cin-Ty Lee and an anonymous reviewer, whose suggestions substantially improved this
665 paper. Discussions with Keith Putirka greatly improved the depth of melting section of the paper. This
666 work was supported by the U.S. National Science Foundation through grant 1016100.
667

Always consult and cite the final, published document. See http://www.minsocam.org or GeoscienceWorld

REFERENCES

Asimow, P.D., and Ghiorso, M.S., (1998) Algorithmic Modifications Extending MELTS to Calculate Subsolidus Phase Relations. American Mineralogist, 83, 1127-1131.

Baker, L., Rutherford, M.J., (1996) The effect of dissolved water on the oxidation state of silicic melts. Geochimica et Cosmochimica Acta, 60, 2179-2187

Balhaus, C., (1993) Redox states of lithospheric and asthenospheric upper mantle. Contributions to Mineralogy and Petrology. 114:331-348.

Barth, M.G., McDonough, W.F., Rudnick, R.L. (2000) Tracking the budget of Nb and Ta in the continental crust. Chemical Geology, 165, 197-213.

Bergman, S., Foland, K., and Spera, F. (1981) On the origin of the amphibole-rich vein in a peridotite inclusion from the Lunar Crater Volcanic Field, Nevada, U.S.A. Earth Planetary Science Letters, 56, 343-361.

Bergman, S.C., (1982) Petrogenetic aspects of the alkali basaltic lavas and included megacrysts and nodules from the Lunar Crater Volcanic Field, Nevada, U.S.A. Ph.D. dissertation, Ohio State University, Columbus, Ohio.

Brenna, M., Cronin, S.J., Smith, I.E., Sohn, Y.K., and Németh, K., (2010) Mechanisms driving polymagmatic activity at a monogenetic volcano, Udo, Jeju Island, South Korea. Contributions to Mineralogy and Petrology, 160, 931-950.

Always consult and cite the final, published document. See http://www.minsocam.org or GeoscienceWorld

693

694 Brenna, M., Cronin, S.J., Smith, I.E.M., Maas, R., and Sohn, Y.K., (2012) How small-volume basaltic
695 magmatic systems develop: a case study from the Jeju Island Volcanic Field, Korea. Journal of
696 Petrology, 53, 985-1018.

697

698 Brown, B., Bursik, M., Deming, J., Louros, M., Martos, A., and Stine, S., (2010) Eruption chronology
699 and petrologic reconstruction of the ca. 8500 yr B.P. eruption of Red Cones, southern Inyo chain,
700 California. Geological Society of America Bulletin, 122, 1401-1422.

701

702 Brown, R.J., and Valentine, G.A., (2013) Physical characteristics of kimberlite and basaltic intraplate
703 volcanism and implications of a biased kimberlite record. Geological Society of America Bulletin,
704 125, 1224-1238.

705

706 Cameron, M., and Papike, J.J., (1981) Structural and chemical variations in pyroxenes. American
707 Mineralogist, 66, 1-50.

708

709 Chazot, G., Menzies, M.A. and Harte, B. (1996) Determination of partition coefficients between
710 apatite, clinopyroxene, amphibole, and melt in natural spinel lherzolites from Yemen: Implications for
711 wet melting of the lithospheric mantle. Geochimica et Cosmochimica Acta, 60, 423-437.

712

713 Connor, C.B., and Conway, F.M., (2000) Basaltic volcanic fields. Encyclopedia of Volcanoes,
714 Academic Press, New York, pp. 331-343.

715

716 Cortés, J. A., Wilson, M., Condliffe, E., Francalanci, L., and Cherkoff, D.G., (2005) The evolution of
717 the magmatic system of Stromboli Volcano during the Vancori period (26-13.8 ky). Journal of

Always consult and cite the final, published document. See http://www.minsocam.org or GeoscienceWorld

718 Volcanology and Geothermal Research, 147, 1-38.

719

720 Cortés, J.A., Wilson, M., Condliffe, E., and Francalanci, L., (2006) The occurrence of forsterite and
721 highly oxidising conditions in basaltic lavas from Stromboli volcano. Italy. Journal of Petrology, 47,
722 1345-1373.

723

724 Cortés, J.A., and Palma, J.L., (2012) PetrologicalINput - Graphical oUtput.
725 https://vhub.org/resources/pingu.

726

727 Deer, W.A., Howie, R.A., and Zussman, J., (1996) An Introduction to the Rock-Forming Minerals (2nd
728 Edition). 712 p, Pearson Education Limited, Essex, England.

729

730 Dickson, L.D., (1997) Volcanology and geochemistry of Pliocene and Quaternary basalts on Citadel
731 Mountain, Lunar Crater Volcanic Field, Pancake Range, Nevada. M.S. Thesis, University of Nevada
732 Las Vegas.

733

734 Erlund, E.J., Cashman, K.V., Wallace, P.J., Pioli, L., Rosi, M., Johnson, E., Delgado-Granados, H.,
735 (2009) Compositional evolution of magma from Paricutín volcano, México. Journal of Volcanology
736 and Geothermal Research, 197, 167-187.

737

738 Farmer, G.L., Perry, F.V., Semken, S., Crowe, B., Curtis, D., and DePaolo, D.J., (1989)
739 Isotopic evidence on the structure and origin of subcontinental lithospheric mantle
740 in southern Nevada. Journal of Geophysical Research, 94, 7885-7898.

741

742 Foland, K.A., and Bergman, S.C., (1992) Temporal and spatial distribution of basaltic volcanism in the

Always consult and cite the final, published document. See http://www.minsocam.org or GeoscienceWorld

743 Pancake and Reveille Ranges north of Yucca Mountain. Proceedings International Nuclear Waste
744 Symposium, 2, American Nuclear Society and American Society of Civil Engineers, 2366-2371.
745
746 Gazel, E., Plank, T., Forsyth, D.W., Bendersky, C., Lee, C.-T. A., and Hauri, E.H., (2012) Lithospheric
747 versus asthenospheric mantle sources at the Big Pine Volcanic Field, California. Geochemistry
748 Geophysics Geosystems, 13, Q0AK06, doi:10.1029/2012GC004060.
749
750 Gilbert, H.J. and Sheehan, A.F. (2004) Images of crustal variations in the intermountain west. Journal
751 of Geophysical Research,109, B03306. doi:10.1029/2003JB002730.
752
753 Ghiorso, M. S., and Sack, R. O., (1995) Chemical Mass Transfer in Magmatic Processes. IV. A Revised
754 and Internally Consistent Thermodynamic Model for the Interpolation and Extrapolation of Liquid-
755 Solid Equilibria in Magmatic Systems at Elevated Temperatures and Pressures. Contributions to
756 Mineralogy and Petrology, 119, 197-212.
757
758 Ghiorso, M. S., Hirschmann, M.M., Reiners, P.W., and Kress, V.C., (2002) The pMELTS: A revision of
759 MELTS aimed at improving calculation of phase relations and major element partitioning involved in
760 partial melting of the mantle at pressures up to 3 GPa. Geochemistry, Geophysics, Geosystems, 3,
761 10.1029/2001GC000217.
762
763 Hammarstrom, J.M., and Zen, E.A., (1986) Aluminium in hornblende—an empirical igneous
764 geobarometer. American Mineralogist, 71, 1297–1313.
765
766 Heizler, M.T., (2013) $^{40}Ar/^{39}Ar$ geochronology results for Lunar Crater Volcanic Field basalts, Nevada.
767 New Mexico Geochronological Research Laboratory Report NMGRL-IR-792.

Always consult and cite the final, published document. See http://www.minsocam.org or GeoscienceWorld

https://vhub.org/resources/2503.

Herzberg, C., (2011) Identification of Source Lithology in the Hawaiian and Canary Islands: Implications for Origins. Journal of Petrology, 52, 113-146.

Herzberg, C., Asimow, P.D., Ionov, D.A., Vidito, C., Jackson, M.G., Geist, D. (2013) Nickel and helium evidence for melt above the core-mantle boundary. Nature, 493, 393-397.

Higgins, M. D., (2006) Quantitative Textural Measurements in Igneous and Metamorphic Petrology. 276 p. Cambridge University Press.

Hintz, A. R., and Valentine, G. A., (2012) Complex plumbing of monogenetic scoria cones: New insights from the Lunar Crater Volcanic Field (Nevada, USA).Journal of Volcanology and Geothermal Research, 239-240, 19-32.

Hirschmann, (2000) Mantle solidus: experimental constraints and the effect of peridotite composition. Geochemistry, Geophysics, Geosystems, 1, doi: 10.1029/2000GC000070.

Johnson, P., Valentine, G.A., Cortés, J.A., Tadini, A. (2014) Basaltic tephra from monogenetic Marcath Volcano, central Nevada. Journal of Volcanology and Geothermal Research, 281, 27-33.

Johnson, E.R., Wallace, P.J., Cashman, K.V., Delgado Granados, H., and Kent, A.J.R., (2008) Magmatic volatile contents and degassing-induced crystallization at Volcán Jorullo, Mexico: implications for melt evolution and the plumbing systems of monogenetic volcanoes. Earth and Planetary Science Letters, 269, 478-487.

Always consult and cite the final, published document. See http://www.minsocam.org or GeoscienceWorld

Kargel, (1986) The geochemistry of basalts and mantle inclusions from the Lunar Crater Volcanic Field, Nevada; petrogenetic and geodynamic implications. M.Sc. Thesis, The Ohio State University.

Kumar, P., Yuan, X., Kind, R., and Mechie, J., (2012) The lithosphere-asthenosphere boundary observed with USArray receiver functions. Solid Earth, 3, 149-159.

Leake, B.E., Woolley, A.R., Arps, C.E.S., Birch, W.D., Gilbert, M.C., Grice, J.D., Hawthorne, F.C., Kato, A., Kisch, H.J., Krivovichev, V.G., Linthout, K., Laird, J., Mandarino, J.A., Maresch, W.V., Nickel, E.H., Rock, N.M.S., Schumacher, J.C., Smith, D.C., Stephenson, N.C.N., Ungaretti, L., Whittaker, E.J.W., and Guo, Y.Z., (1997) Nomenclature of amphiboles: report of the subcommittee on amphiboles of the international mineralogical association, commission on new minerals and mineral names. American Mineralogist, 82, 1019–1037

Lee, C.A., Luffi, P., Plank, T., Dalton, H., and Leeman, W.P. (2009) Constraints on the depths and temperatures of basaltic magma generation on Earth and other terrestrial planets using new thermobarometers for mafic magmas. Earth and Planetary Science Letters, 279, 20-33.

Le Maitre R.W., Streckeisen, A., Zanettin, B., Le Bas, M.J., Bonin, B., Bateman, P., Bellieni, G., Dudek, A., Efremova, S., Keller, J., Lamere, J., Sabine, P.A., Schmid, R., Sorensen, H., and Woolley, A.R., (2002) Igneous Rocks: A Classification and Glossary of Terms, Recommendations of the International Union of Geological Sciences, Subcommission of the Systematics of Igneous Rocks. 256 p. Cambridge University Press.

Loucks, R. (1996) A precise Olivine-Augite Mg-Fe-exchange geothermometer. Contributions to

Always consult and cite the final, published document. See http://www.minsocam.org or GeoscienceWorld

Mineralogy and Petrology, 125, 140-150.

Luhr, J.F., and Simkin, T., (1993) Paricutín: The Volcano Born in a Mexican Cornfield. 441 p. Geoscience Press, Inc., Phoenix, Arizona.

Luhr, J.F., Aranda-Gómez, J.J., and Housh, T.B., (1995) San Quintín volcanic field, Baja California Norte, México: Geology, petrology, and geochemistry. Journal of Geophysical Research, 100, 10353-10380.

Lum, C.C.L., (1986) Aspects of petrogenesis of alkali basalts from the Lunar Crater Volcanic Field, Nevada. M.S. thesis, Ohio State University, Columbus, Ohio.

Lum, C.C.L., and Leeman, W.P., (1989) Isotopic variation in continental basaltic lavas as indicators of mantle heterogeneity: Examples from the Western U.S. Cordillera. Journal of Geophysical Research, 94, B6, 7871-7884.

Maaløe, S., (2011) Olivine phenocrysts growth in Hawaiian tholeiites: evidence for supercooling. Journal of Petrology, 7-8, 1579-1589

Marsh, B.D., (1988) Crystal size distribution (CSD) in rocks and the kinetics and dynamics of crystallization I. Theory: Contributions to Mineralogy and Petrology, 99, 277–291.

Marsh, B.D., (1998) On the interpretation of crystal size distributions in magmatic systems: Journal of Petrology, 39, 553–600.

Always consult and cite the final, published document. See http://www.minsocam.org or GeoscienceWorld

McGee, L.E., Smith, I.E.M., Millet, M.-A., Handley, H.K., and Lindsay, J.M., (2013) Asthenospheric control on melting processes in a monogenetic basaltic system: a case study of the Auckland Volcanic Field, New Zealand. Journal of Petrology, doi:10.1093/petrology/egt043.

Mayer, B., Jung, S., Romer, R.L., Pfänder, J.A., Klügel, A., Pack, A., Gröner, E., (2014). Amphibole in alkaline basalts from intraplate settings: implications for the petrogenesis of alkaline lavas from the metasomatized lithospheric mantle. Contributions to Mineralogy and Petrology, 167:989, doi: 10.1007/s00410-014-0989-3

Menzies, M.A., (1989) Cratonic, circumcratonic, and oceanic mantle domains beneath the Western United States. Journal of Geophysical Research, 94(B6), 7899-7915, doi: 10.06.1989

Mock, A., and Jerram, D.A., (2005) Crystal Size Distributions (CSD) in three dimensions: Insights from the 3D reconstruction of a highly porphyritic rhyolite. Journal of Petrology, 46,1525-1541.

Morgan, D. J. and Jerram, D. A., (2006) On estimating crystal shape for crystal size distribution analysis. Journal of Volcanology and Geothermal Research, 154, 1-7.

Morimoto, N., (1989) Nomenclature of Pyroxenes. Canadian Mineralogist, 27, 143-156

Muffler, L.J.P., Clynne, M.A., Calvert, A.T., and Champion, D.E., (2011) Diverse, discrete, mantle-derived batches of basalt erupted along a short normal fault zone: the Poison Lake chain, southernmost Cascades. Geological Society of America Bulletin, 123, 2177-2200.

Naumann, T.R., Smith, E.I., Shafiqullah, M., Damon, P.E., (1991) New ages for Pliocene mafic to

Always consult and cite the final, published document. See http://www.minsocam.org or GeoscienceWorld

intermediate volcanic rocks in the Reveille Range, Nevada. Isochron/West, 57, 12-16.

Nicholis, M.G., and Rutherford, M.J., (2004) Experimental constraints on magma ascent rate for the Crater Flat volcanic zone hawaiite. Geology, 32, 489-492.

Nimis, P. and Ulmer, P. (1998) Clinopyroxene geobarometry of magmatic rocks. Part 1: An expanded structural geobarometer for anhydrous and hydrous, basic and ultrabasic systems. Contributions to Mineralogy and Petrology, 133, 122-135.

Nimis, P., (1999) Clinopyroxene geobarometry of magmatic rocks. Part 2. Structural geobarometers for basic to acid, tholeiitic and mildly alkaline magmatic systems. Contributions to Mineralogy and Petrology, 135, 62-74.

Papike, J.J., Cameron, K.L., Baldwin, K. (1974) Amphiboles and pyroxenes: Characterization of OTHER than quadrilateral components and estimates of ferric iron from microprobe data. Geological Society of America, Abstracts with Programs, 6, 1053-1054.

Petermann. M., and Hirschmann, M.M., (2003) Partial melting experiments on a MORB-like pyroxenite between 2 and 3 GPa: Constraints on the presence of pyroxenite in basalt source regions from solidus location and melting rate. Journal of Geophysical Research, 108(B2,2125), doi: 10.1029/2000JB000118.

Pioli, L., Erlund, E., Johnson, E., Cashman, K., Wallace, P., Rosi, M., and Delgado-Granados, H., (2008) Explosive dynamics of violent Strombolian eruptions: The eruption of Paricutín Volcano 1943-1952 (México). Earth and Planetary Science Letters, 271, 359-368.

Always consult and cite the final, published document. See http://www.minsocam.org or GeoscienceWorld

Powell, M., and Powell, R., (1974) An olivine-clinopyroxene geothermometer. Contributions to Mineralogy and Petrology, 48, 249-263.

Putirka, K., (2008) Thermometers and barometers for volcanic systems. Reviews in Mineralogy and Geochemistry, 69, 61-120

Putirka, K., Jean, M., Cousens, B., Sharma, Rl, Torrez, G, and Carlson, C., (2012) Cenozoic volcanism in the Sierra Nevada and Walker Lane, California, and a new model for lithospheric degradation. Geosphere, 8, 265-291, doi: 10.1130/GES00728.1.

Ridolfi, F,. Renzulli, A,. and Puerini, M., (2010) Stability and chemical equilibrium of amphibole in calc-alkaline magmas: an overview, new thermobarometric formulations and application to subduction-related volcanoes. Contributions to Mineralogy and Petrology, 160, 45–66, doi:10.1007/s00410-009-0465-7

Ridolfi, F., and Renzulli, A., (2012) Calcic amphiboles in calc-alkaline and alkaline magmas: thermobarometric and chemometric empirical equations valid up to 1,130°C and 2.2 GPa. Contributions to Mineralogy and Petrology, 163, 877-895.

Rowe, M.C., Peate, D.W., and Peate, I.U., (2011) An investigation into the nature of the magmatic plumbing system at Paricutin Volcano, Mexico. Journal of Petrology, 52, 2187-2220

Scott, D., and Trask, N.J., (1971) Geology of the Lunar Crater Volcanic Field, Nye County, Nevada.

Always consult and cite the final, published document. See http://www.minsocam.org or GeoscienceWorld

914 USGS Professional Paper 599-I, 11-22.

915

916 Shepard, M. K., Arvidson, R. E., Caffee, M., Finkel, R., and Harris, L., (1995) Cosmogenic exposure
917 ages of basalt flows; Lunar Crater volcanic field, Nevada. Geology, 23, 21-24.

918

919 Simakin, A., Zakrevskaya, O., and Salova, T., (2012a) Novel amphibole geo-barometer with
920 application to mafic xenoliths. Earth Science Research, 1, doi: 10.5539/esr.vln2p82

921

922 Simakin, A.G., Salova, T.P., Bondarenko, G.V., (2012b) Experimental study of magmatic melt
923 oxidation by CO_2. Petrology, 20(7), 593-606.

924

925 Smith, R.L., and Luedke, R.G., (1984) Potentially active volcanic lineaments and loci in the western
926 conterminous Unites States. In Explosive volcanism: Inception, evolution, and hazards: Studies in
927 Geophysics, National Academy Press, Washington DC, p. 47-66.

928

929 Smith, I.E.M., Blake, S., Wilson, C.J.N., and Houghton, B.F., (2008) Deep-seated fractionation during
930 the rise of a small-volume basalt magma batch: Crater Hill, Auckland, New Zealand. Contributions to
931 Mineralogy and Petrology, 155, 511-527.

932

933 Smith, D., (2000) Insights into the evolution of the uppermost continental mantle from xenolith
934 localities on and near the Colorado Plateau and regional comparisons. Journal of Geophysical
935 Research, 105, 16769-16781

936

937 Sobolev, A.V., Hoffmann, A.W., Kuzmin, D.V., Yaxley, G.M., Arnt, N.T., Chung, S., Danyushevsky,
938 L. V., Elliott, T., Frey, F.A., Garcia, M.O., Gurenko, A.A., Kamenetsky, V.S., Kerr, A.C.,

Always consult and cite the final, published document. See http://www.minsocam.org or GeoscienceWorld

939 Krivolutskaya, N.A., Matvienkov, V.V., Nikogozian, I.K., Rocholl, A., Sigurdsson, I.A.,
940 Sushchevskaya, N. M., Teklay, M., (2007) The amount of recycled crust in sources of mantle-derived
941 melts. Science 316, 412-417.
942
943 Stickney, E.K., (2004) The volcanology and petrogenesis of the northern Lunar Crater Volcanic Field,
944 Nye County, Nevada. M.Sc. Thesis. University of Nevada, Las Vegas.
945
946 Sun, S.S., and McDonough, W.F., (1989) Chemical and isotopic systematics of oceanic basalts:
947 implications for mantle composition and processes. Geological Society of London, Special
948 Publications, 42, 313-345.
949
950 Thirwall, M.F., Upton, B.G.J., and Jenkins, C. (1994) Interaction between continental lithosphere and
951 the Iceland plume-Sr-Nd-Pb isotope geochemistry of Tertiary basalt, NE Greenland. Journal of
952 Petrology, 35, 839-879.
953
954 Tuff, J., Takahashi, E., and Gibson, S.A., (2005) Experimental constraints on the role of garnet
955 pyroxenite in the genesis of high-Fe mantle plume derived melts. Journal of Petrology, 46, 2023-2058.
956
957 Valentine, G.A., and Cortés, J.A., (2013) Time and space variations in magmatic and phreatomagmatic
958 eruptive processes at Easy Chair (Lunar Crater Volcanic Field, Nevada, USA). Bulletin of Volcanology,
959 75, doi:10.1007/s00445-013-0752-z.
960

Always consult and cite the final, published document. See http://www.minsocam.org or GeoscienceWorld

961 Valentine, G.A., and Gregg, T.K.P., (2008) Continental basaltic volcanoes — Processes and problems.
962 Journal of Volcanology and Geothermal Research, 177, 857-873.
963
964 Valentine, G.A., and Hirano, H., (2010) Mechanisms of low-flux intraplate volcanic fields – Basin and
965 Range (North America) and northwest Pacific Ocean. Geology, 38, 55-58.
966
967 Valentine, G.A., and Keating, G.N., (2007) Eruptive styles and inferences about plumbing systems at
968 Hidden Cone and Little Black Peak scoria cone volcanoes (Nevada, U.S.A.) Bulletin of Volcanology,
969 70, 105-113.
970
971 Valentine, G.A., and Perry, F.V., (2006) Decreasing magmatic footprints of individual volcanoes in a
972 waning basaltic field. Geophysical Research Letters, 33, L14305.
973
974 Valentine, G.A., and Perry, F.V., (2007) Tectonically controlled, time-predictable basaltic volcanism
975 from a lithospheric mantle source (central Basin and Range Province, USA). Earth and Planetary
976 Science Letters, 261, 201-216.
977
978 Valentine, G.A., Shufelt, N.L., and Hintz, A.R.L., (2011) Models of maar volcanoes, Lunar Crater
979 (Nevada, USA). Bulletin of Volcanology, 73, 753-765.
980
981 Vaniman, D.T., Crowe, B.M., and Gladney, E.S., (1982) Petrology and geochemistry of hawaiite lavas
982 from Crater Flat, Nevada. Contributions to Mineralogy and Petrology, 80, 341-357.
983

Always consult and cite the final, published document. See http://www.minsocam.org or GeoscienceWorld

Wade, J., Wood, B.J., (2005) Core formation and the oxidation state of the Earth. Earth and Planetary Science Letters, 236, 78-95.

Wang, K, Plank, T., Walker, J.D., Smith, E.I., (2001) A mantle melting profile across the Basin and Range, SW USA. Journal of Geophysical Research, 107(B1), doi: 10.1029/2001JB000209.

White, J.D.L., and Ross, P.-S., (2011) Maar-diatreme volcanoes: a review. Journal of Volcanology and Geothermal Research, 201, 1-29.

Yogodzinski, G. M., Naumann, T.R., Smith, E.I., Bradshaw, T.K., and Walker, J.D., (1996) Evolution of a mafic volcanic field in the central Great Basin, south central Nevada. Journal of Geophysical Research, 101(B8), 17425-17445.

Always consult and cite the final, published document. See http://www.minsocam.org or GeoscienceWorld

997 **Figure Captions**
998

999 Figure 1: Location of the Lunar Crater Volcanic Field in the western U.S.A. and the State of Nevada
1000 showing the Pancake and Reveille Range within the volcanic field. Dashed lines are the main roads in
1001 the area. Red box encompasses the study area (see Figure 2).

1002

1003 Figure 2: Simplified geological map of the northern part of the Lunar Crater Volcanic Field,
1004 highlighting the four volcanoes studied in this work. Outline of tephra deposits from Johnson (2013).

1005

1006 Figure 3: Total Alkali versus silica diagram according to Le Maitre et al. (2002). Hi Desert basalt
1007 (Qhib) open circle, Mizpah basalt (Qmzb) open square, Giggle Spring basalt (Qgsb) asterisk, Marcath
1008 volcano products (Qm) crosses. All whole-rock figures plotted using PINGU (Cortés and Palma, 2011).

1009

1010 Figure 4: Whole-rock major element variation diagrams versus MgO for the samples of this study.
1011 Symbols as in Figure 3.

1012

1013 Figure 5: Rare Earth Element diagram normalized according to Sun and McDonough (1989). Symbols
1014 as in Figure 3.

1015

1016 Figure 6: Spider diagrams normalized according to OIB from Sun and McDonough (1989). Symbols as
1017 in Figure 3.

1018

1019 Figure 7: a) La/Yb vs. Zr/Nb b) Rb/Zr vs. Ni/Zr c) La/Yb vs. Dy/Yb. Symbols as in Figure 3.

1020

Always consult and cite the final, published document. See http://www.minsocam.org or GeoscienceWorld

Figure 8: a) La/Nb vs Nb [ppm] b) Nb/Ta vs Nb [ppm]. Fields as defined in Barth et al., (2000). Symbols as in Figure 3.

Figure 9: Mineral classification based on mineral chemistry for a) olivine (Deer et al., 1996) b) pyroxenes (Morimoto, 1989) c) plagioclase (Deer et al., 1996) and d) amphiboles (Leake, 1997) from electron microprobe analyses in the studied samples. Symbols of the units as in Figure 3.

Figure 10: (a) Fe^{2+}/Mn vs. %Fo=Mg/(Mg+Fe^{2+}+Mn) and (b) 100xMn/Fe^{2+} vs. 100xCa/Fe^{2+} (%Fo>85) in mineral chemistry analyses of olivine recalculated as cation per formula unit from electron microprobe analyses. Symbols of the units as in Figure 3.

Figure 11. Natural logarithm of the density population (mm^{-4}) vs. size (mm) plots of the crystal size distribution for a) olivine b) clinopyroxene c) plagioclase and d) spinel in the studied samples. Minimum crystal sizes that can be measured using ImageJ in an SEM image are ~10-20 pixels long, equivalent to ~5% of the average scale bar of ~300 pixels (around ~0.01-0.02 mm in most of our images except images for measuring oxides with minimum sizes of 0.001-0.002 mm). Black asterisk: Giggle Spring basalt (Qgsb) sampled at the vent. Light grey asterisk: Giggle Spring basalt (Qgsb) lava. Black open squares: Mizpah basalt (Qmzb), Black crosses: Marcath volcano products (Qm).

Figure 12: La/Yb vs. Dy/Yb plots with different models of partial melting of a mantle source. Data points are normalized with C1 chondrite (Sun and McDonough 1989), symbols as in Figure 3. (a) Partial melting of lherzolite source: grey line and filled triangles is a model of batch melting of a garnet lherzolite with 11.5 % of garnet; black line with filled circles is a model of batch melting of a garnet lherzolite with 6% of garnet, black line with open squares is a model of batch melting of a garnet lherzolite with 2% of garnet, black line with open triangles is a model of batch melting of a spinel

Always consult and cite the final, published document. See http://www.minsocam.org or GeoscienceWorld

lherzolite. Tick marks on all curves are at 5% melting intervals. (b) Partial melting of pyroxenite source: black line and filled triangles is a model of batch melting of a garnet pyroxenite with 11% garnet; black line with filled circles is a model of batch melting of a garnet pyroxenite with 9% garnet, black line with open squares models batch melting of a garnet pyroxenite with 5% garnet. Tick marks on all curves are at 5% melting intervals.

Always consult and cite the final, published document. See http://www.minsocam.org or GeoscienceWorld

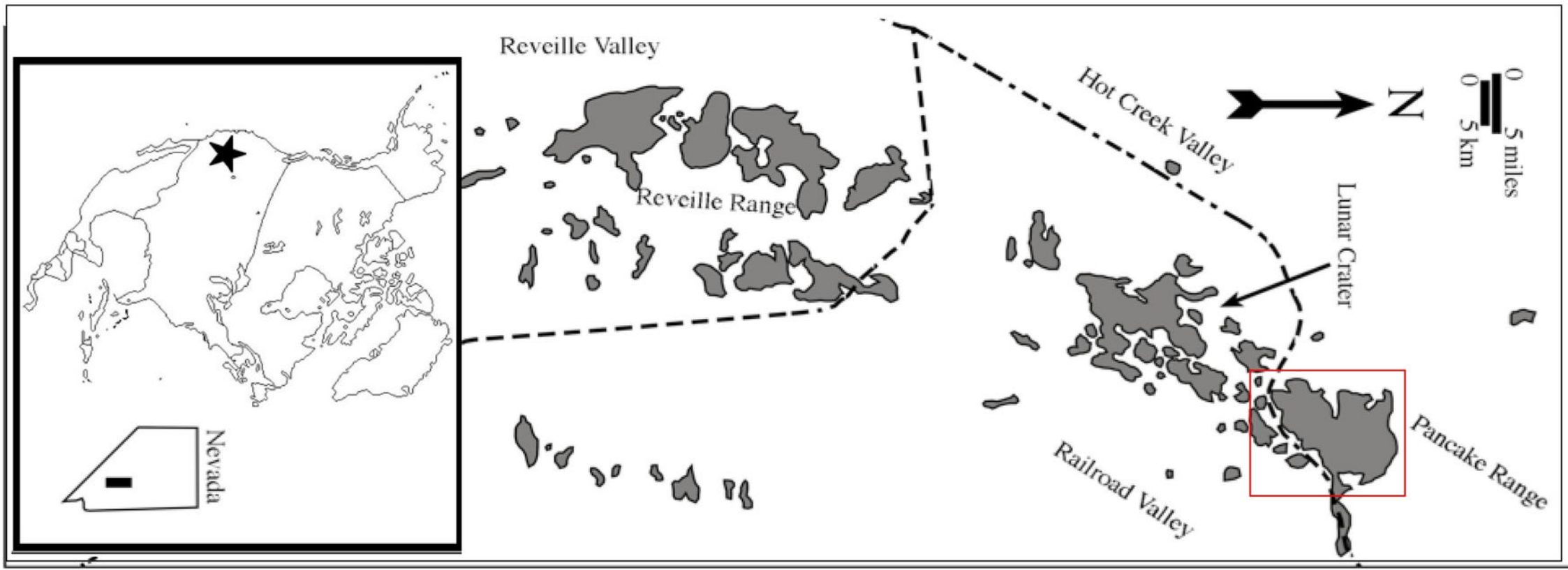
Reveille Valley
Reveille Range
Hot Creek Valley
Lunar Crater
Railroad Valley
Pancake Range
N
0
5 miles
0
5 km
Nevada

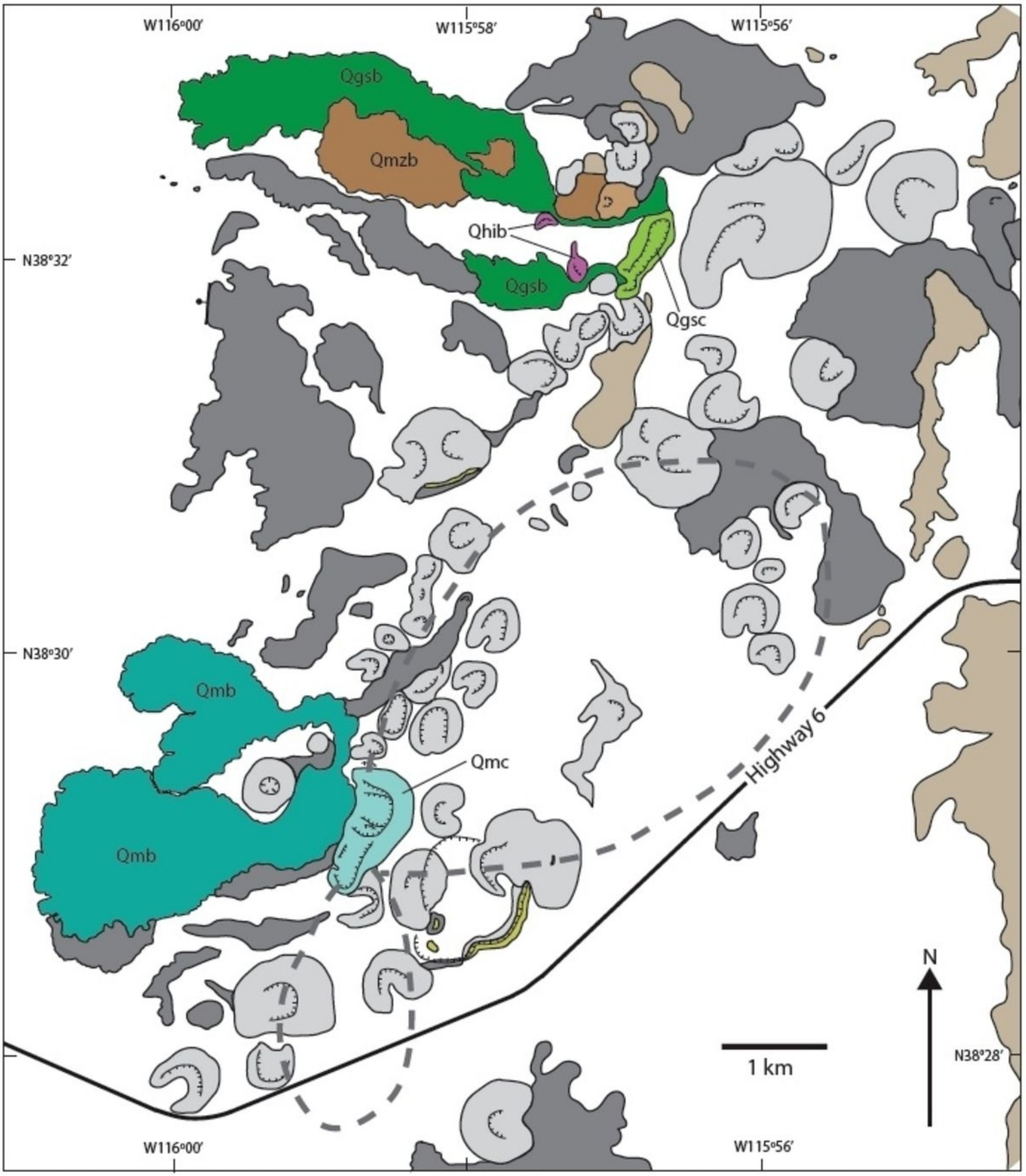

Studied units

- Qmc / Qmb — Marcath basalt (3 ± 10 ka); Qmb - lava; Qmc - pyroclastic cone
- Qgsc / Qgsb — Giggle Spring basalt (< 80 ka); Qgsb - lava; Qgsc - pyroclastic cone
- Qhib — Hi Desert basalt (two agglomerate cones)
- Qmzc / Qmzb — Mizpah basalt (620-740 ka); Qmzb - lava; Qmzc - pyroclastic cone

Other units

- Quaternary alluvium, colluvium, and eolian deposits (locally includes tephra)
- Quaternary basalt (undifferentiated). Lavas dark grey, pyroclastic cones light grey
- Quaternary lapilli tuff and tuff breccia
- Oligocene-Miocene silicic volcanic rocks

- Approximate outer limits of continuous tephra (Marcath)
- Crater rim
- Normal fault (bar on hanging wall)

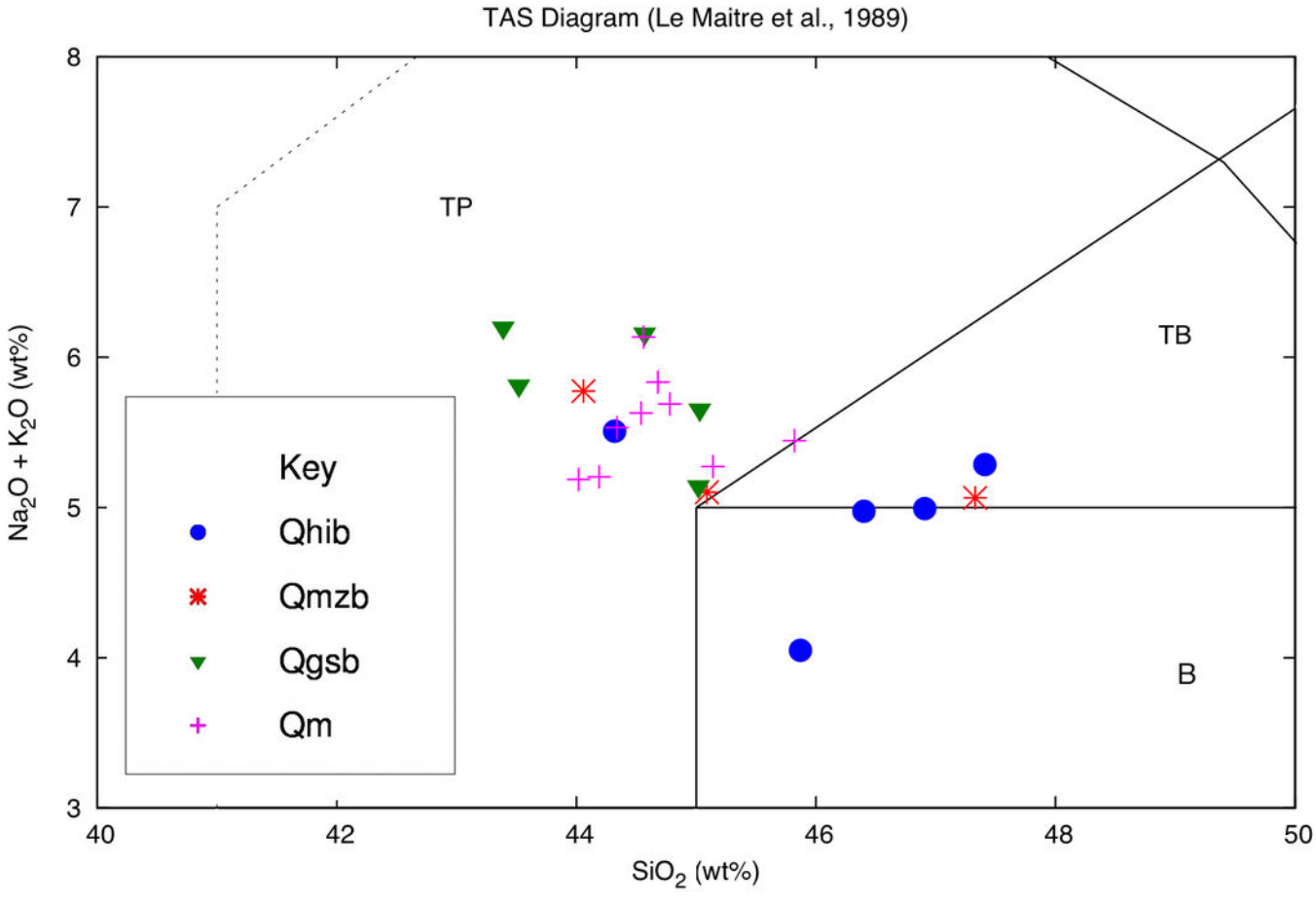
TAS Diagram (Le Maitre et al., 1989)
TP
TB
B
Key
Qhib
Qmzb
Qgsb
Qm
Na2O + K2O (wt%)
SiO2 (wt%)
8
7
6
5
4
3
40
42
44
46
48
50

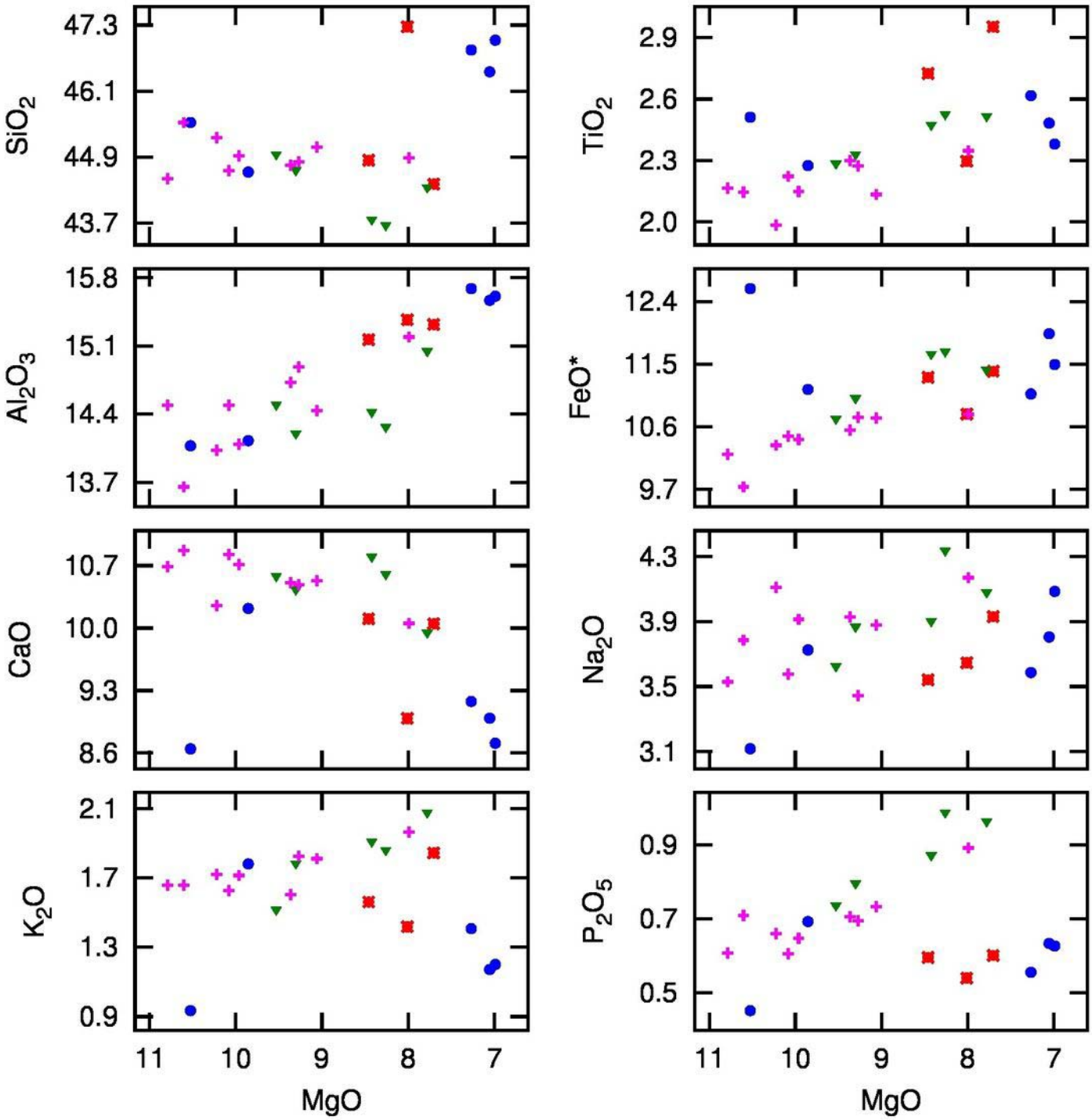
SiO2
47.3
46.1
44.9
43.7
TiO2
2.9
2.6
2.3
2.0
Al2O3
15.8
15.1
14.4
13.7
FeO*
12.4
11.5
10.6
9.7
CaO
10.7
10.0
9.3
8.6
Na2O
4.3
3.9
3.5
3.1
K2O
2.1
1.7
1.3
0.9
P2O5
0.9
0.7
0.5
11
10
9
8
7
MgO
MgO

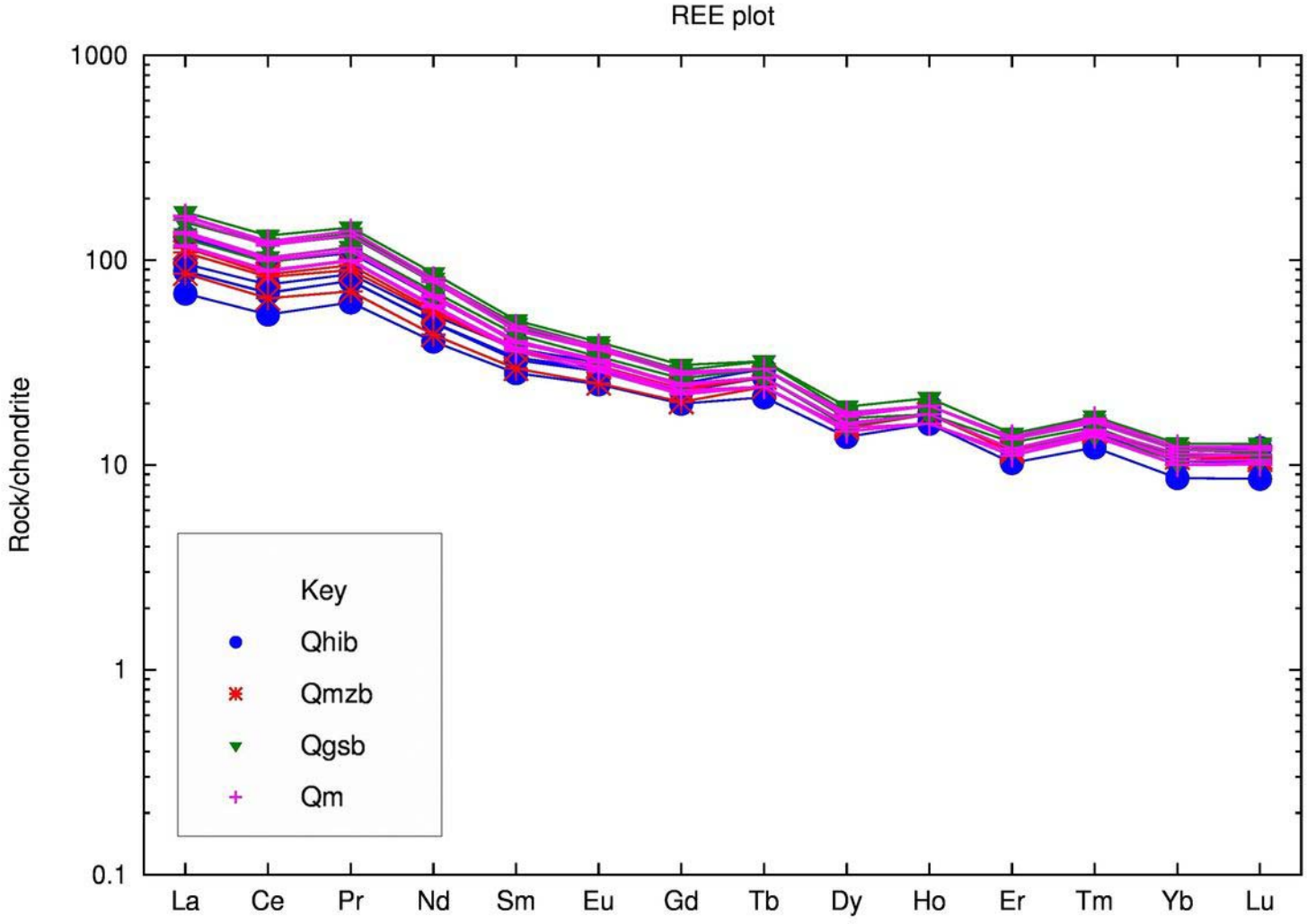
REE plot
1000
100
10
1
0.1
Rock/chondrite
La
Ce
Pr
Nd
Sm
Eu
Gd
Tb
Dy
Ho
Er
Tm
Yb
Lu
Key
Qhib
Qmzb
Qgsb
Qm

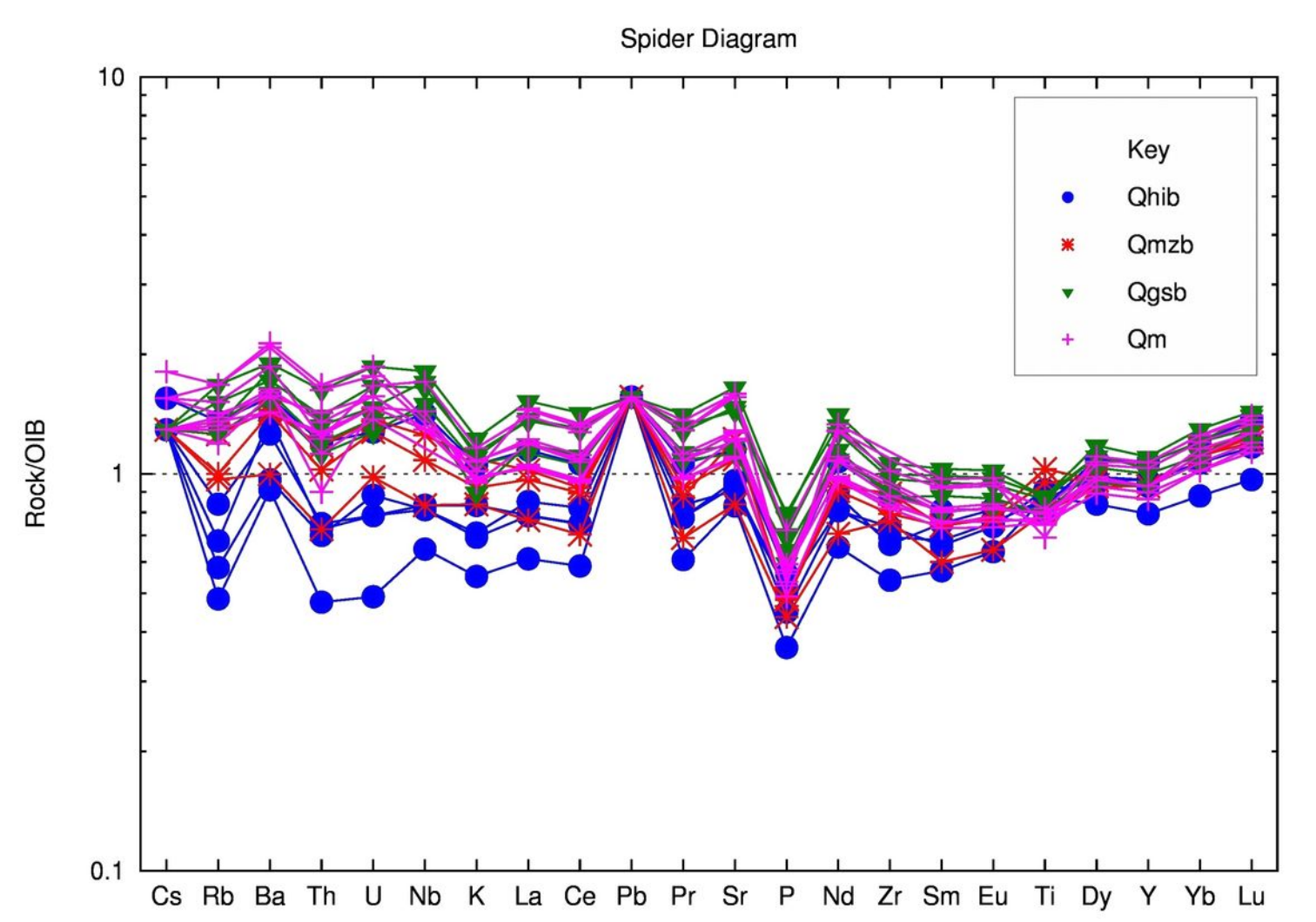
Spider Diagram
10
1
0.1
Rock/OIB
Key
Qhib
Qmzb
Qgsb
Qm
Cs
Rb
Ba
Th
U
Nb
K
La
Ce
Pb
Pr
Sr
P
Nd
Zr
Sm
Eu
Ti
Dy
Y
Yb
Lu

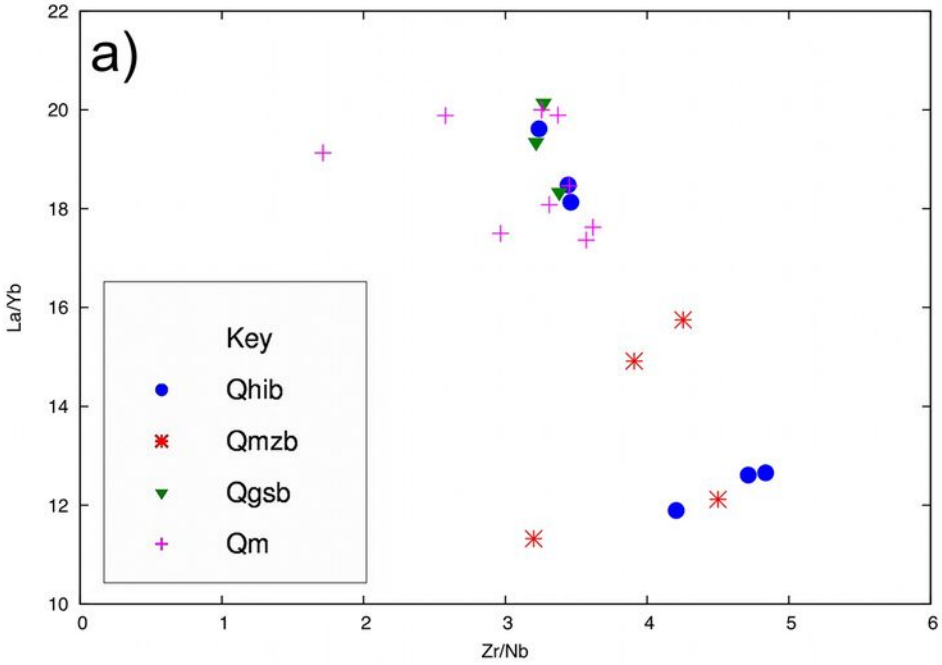
a)
Key
Qhib
Qmzb
Qgsb
Qm
La/Yb
Zr/Nb
22
20
18
16
14
12
10
0
1
2
3
4
5
6

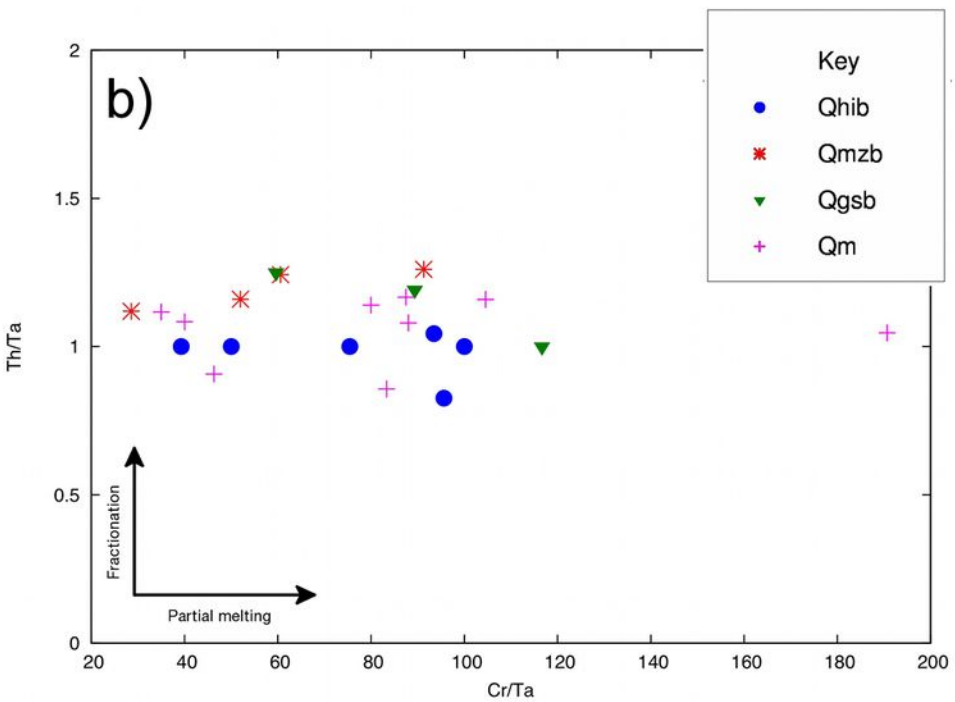
b)
Key
Qhib
Qmzb
Qgsb
Qm
Th/Ta
Cr/Ta
Fractionation
Partial melting
2
1.5
1
0.5
0
20
40
60
80
100
120
140
160
180
200

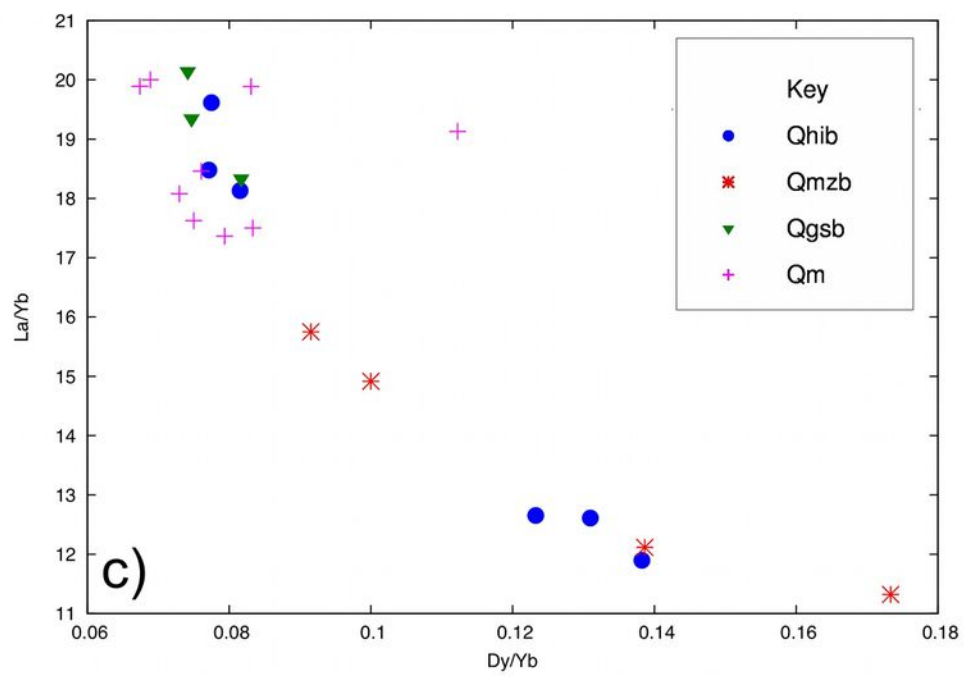
c)
Key
Qhib
Qmzb
Qgsb
Qm
La/Yb
Dy/Yb
21
20
19
18
17
16
15
14
13
12
11
0.06
0.08
0.1
0.12
0.14
0.16
0.18

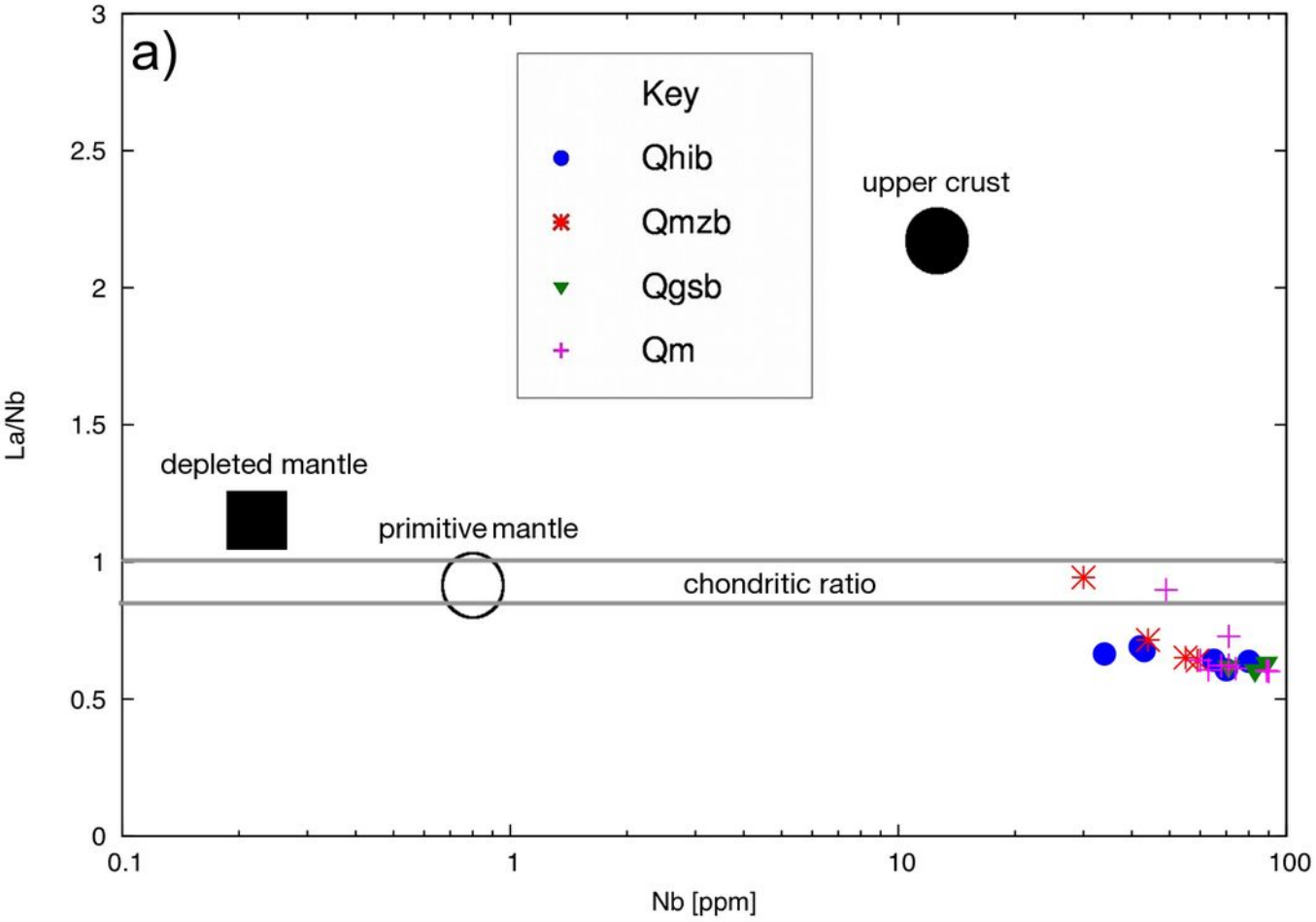
a)
Key
Qhib
Qmzb
Qgsb
Qm
upper crust
depleted mantle
primitive mantle
chondritic ratio
La/Nb
Nb [ppm]
0
0.5
1
1.5
2
2.5
3
0.1
1
10
100

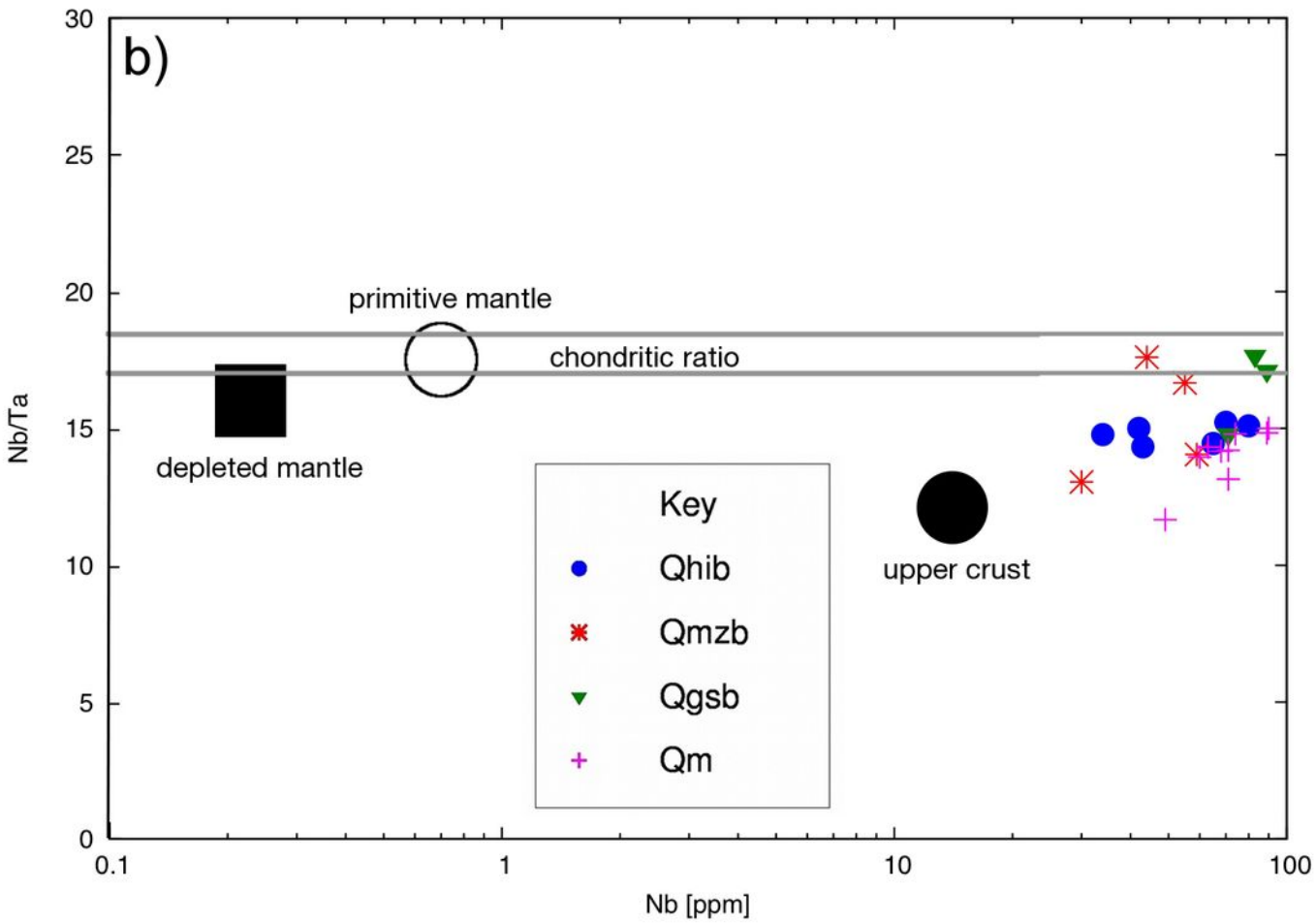
b)
primitive mantle
chondritic ratio
depleted mantle
Key
Qhib
Qmzb
Qgsb
Qm
upper crust
Nb/Ta
Nb [ppm]
0
5
10
15
20
25
30
0.1
1
10
100

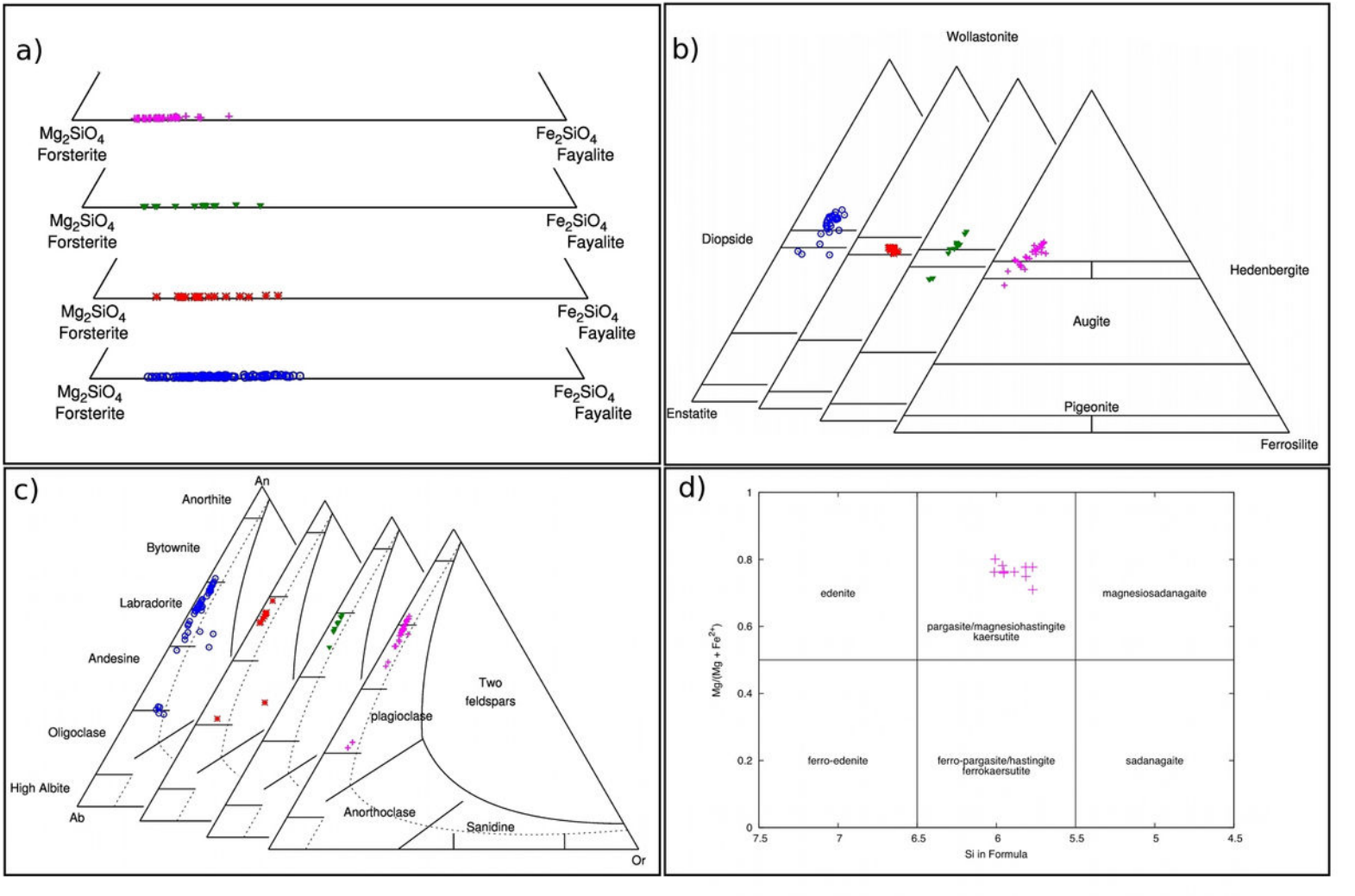
a)
Mg_2SiO_4 Forsterite
Fe_2SiO_4 Fayalite
Mg_2SiO_4 Forsterite
Fe_2SiO_4 Fayalite
Mg_2SiO_4 Forsterite
Fe_2SiO_4 Fayalite
Mg_2SiO_4 Forsterite
Fe_2SiO_4 Fayalite
b)
Wollastonite
Diopside
Hedenbergite
Augite
Enstatite
Pigeonite
Ferrosilite
c)
An
Anorthite
Bytownite
Labradorite
Andesine
Oligoclase
High Albite
Ab
Two feldspars
plagioclase
Anorthoclase
Sanidine
Or
d)
edenite
pargasite/magnesiohastingite kaersutite
magnesiosadanagaite
ferro-edenite
ferro-pargasite/hastingite ferrokaersutite
sadanagaite
$Mg/(Mg + Fe^{2+})$
Si in Formula
1
0.8
0.6
0.4
0.2
0
7.5
7
6.5
6
5.5
5
4.5

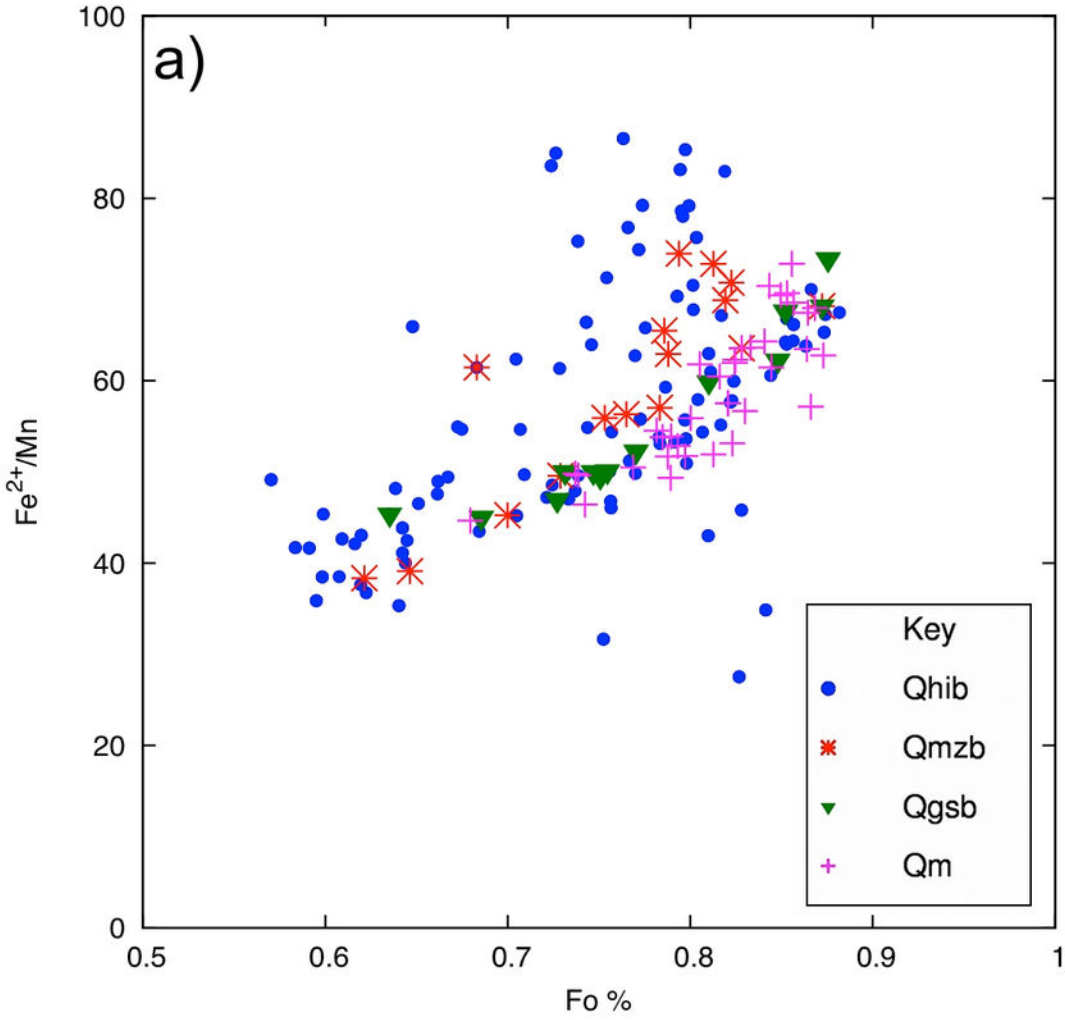
a)
100
80
60
40
20
0
0.5
0.6
0.7
0.8
0.9
1
Fe2+/Mn
Fo %
Key
Qhib
Qmzb
Qgsb
Qm

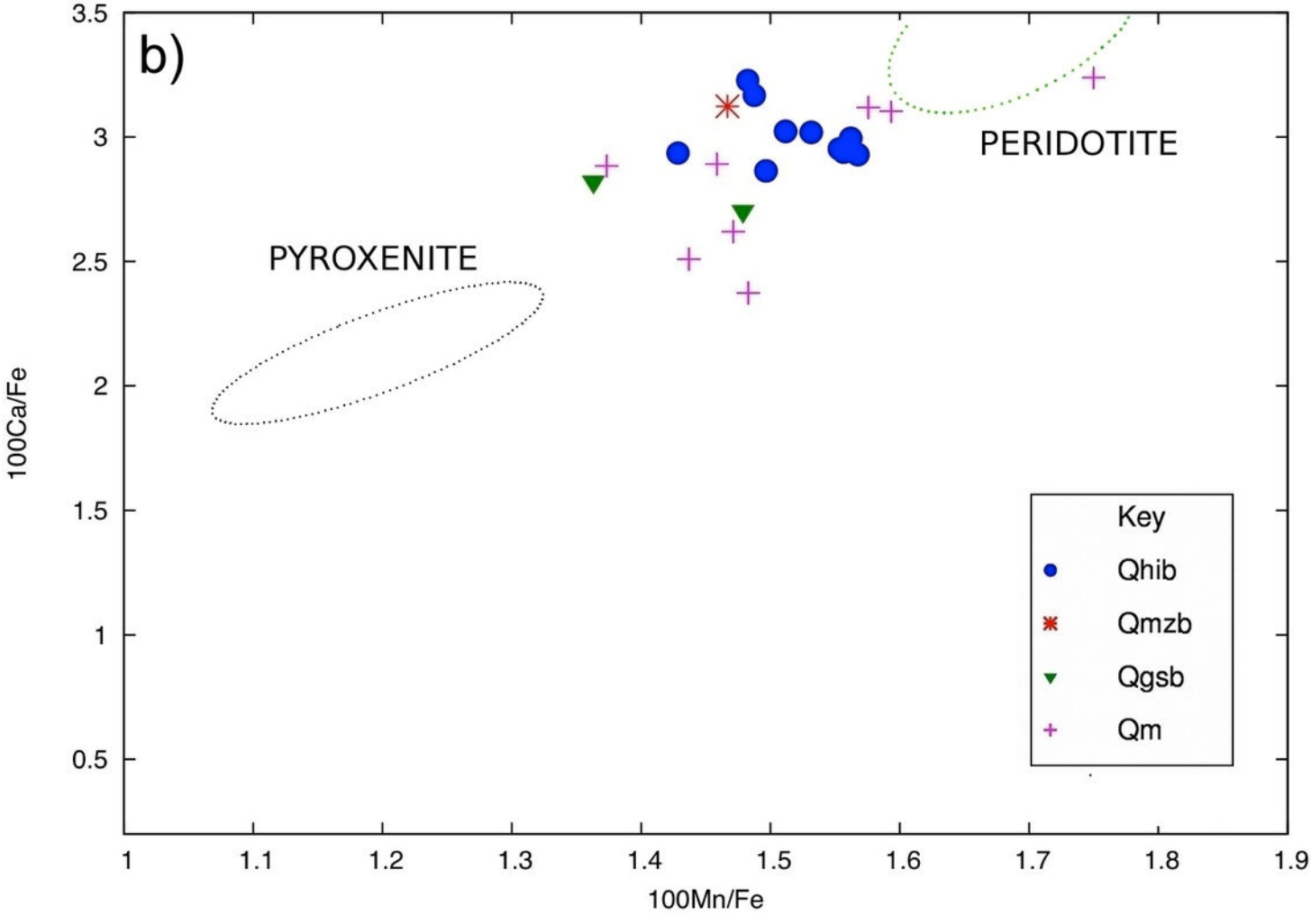
b)
3.5
3
2.5
2
1.5
1
0.5
1
1.1
1.2
1.3
1.4
1.5
1.6
1.7
1.8
1.9
100Ca/Fe
100Mn/Fe
PERIDOTITE
PYROXENITE
Key
Qhib
Qmzb
Qgsb
Qm

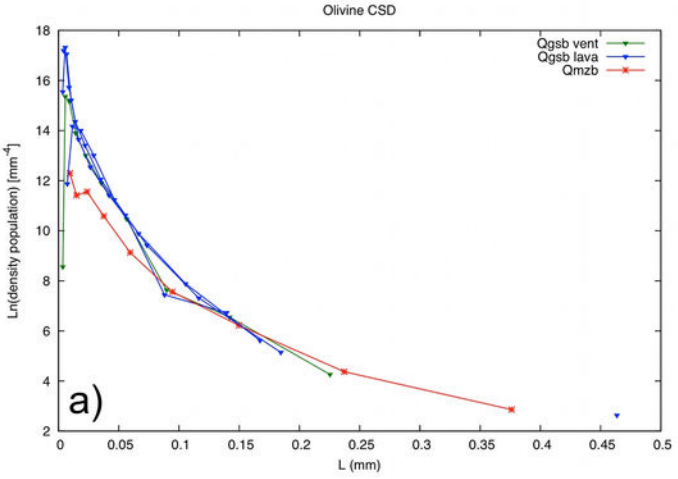
Olivine CSD
Qgsb vent
Qgsb lava
Qmzb
Ln(density population) [mm-4]
L (mm)
a)

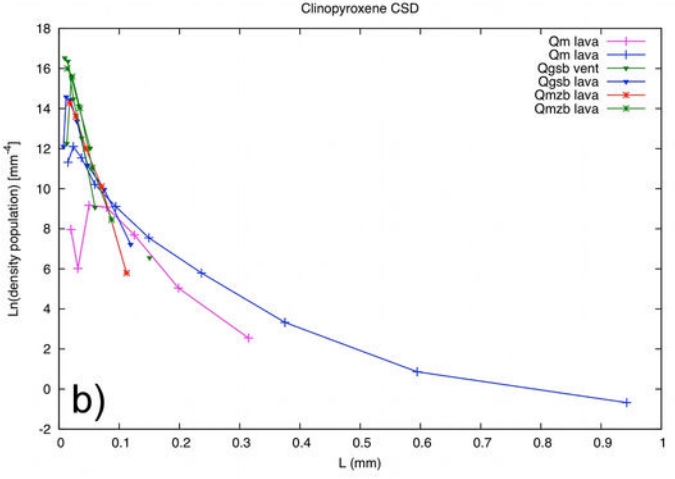
Clinopyroxene CSD
Qm lava
Qm lava
Qgsb vent
Qgsb lava
Qmzb lava
Qmzb lava
Ln(density population) [mm-4]
L (mm)
b)

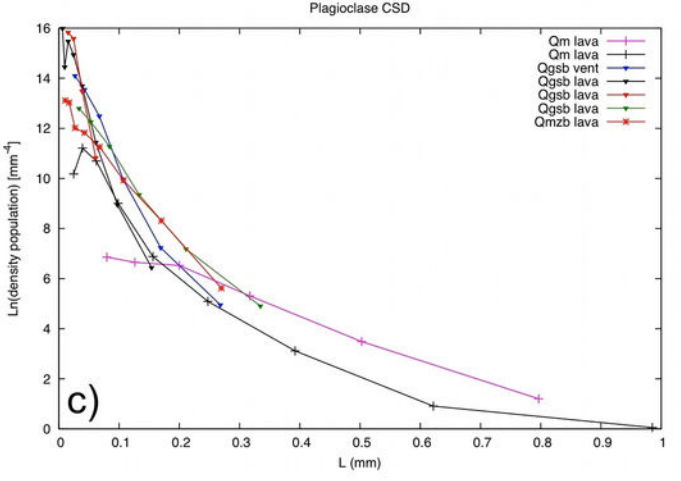
Plagioclase CSD
Qm lava
Qm lava
Qgsb vent
Qgsb lava
Qgsb lava
Qgsb lava
Qmzb lava
Ln(density population) [mm-4]
L (mm)
c)

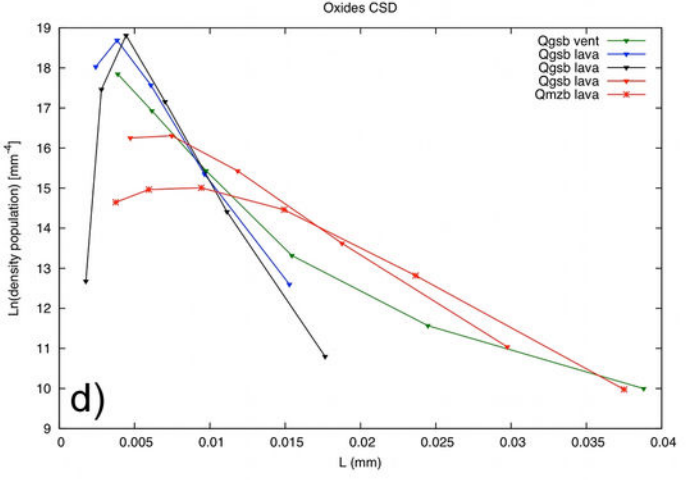
Oxides CSD
Qgsb vent
Qgsb lava
Qgsb lava
Qgsb lava
Qmzb lava
Ln(density population) [mm-4]
L (mm)
d)

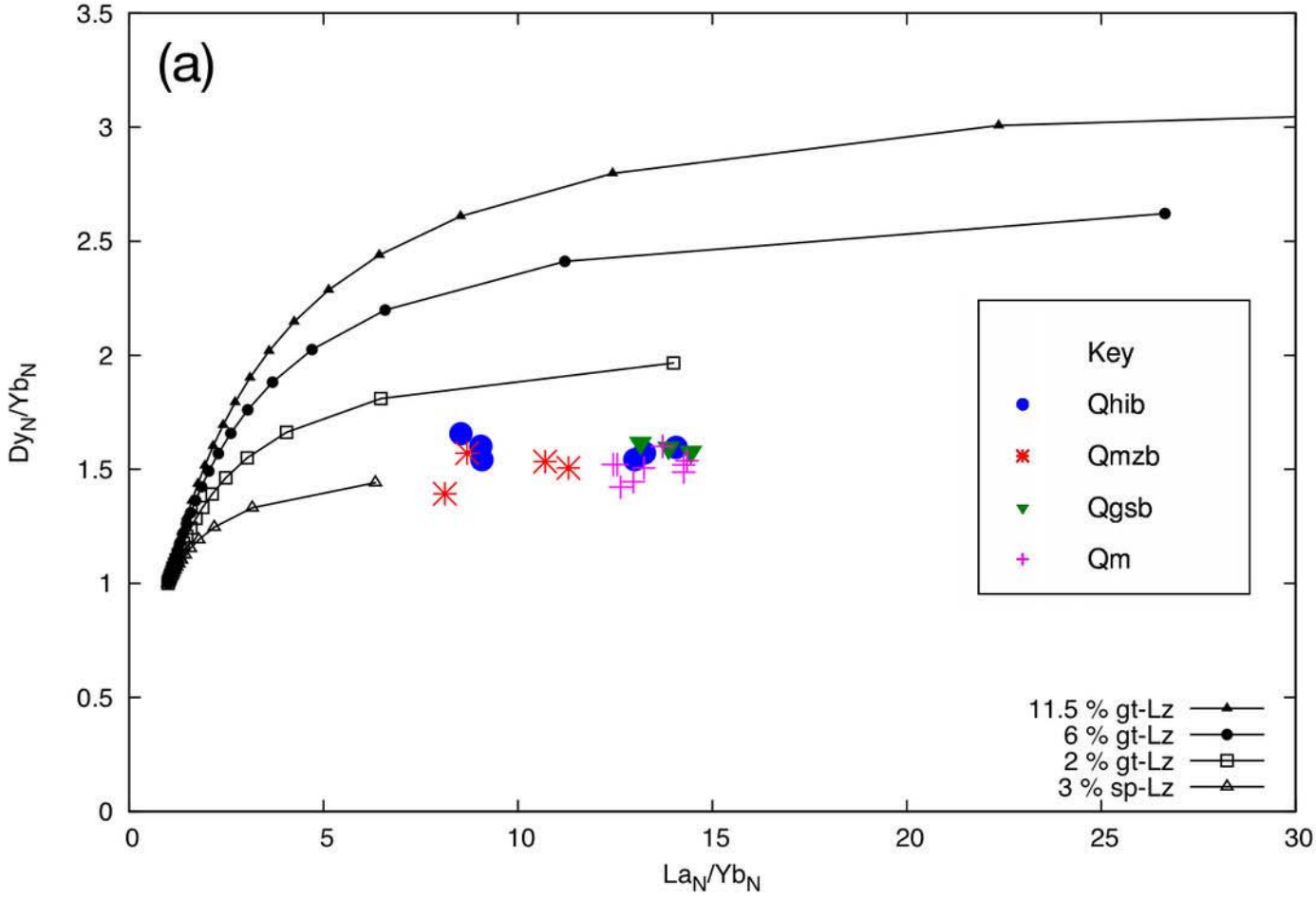
(a)
Key
Qhib
Qmzb
Qgsb
Qm
11.5 % gt-Lz
6 % gt-Lz
2 % gt-Lz
3 % sp-Lz
Dy_N/Yb_N
La_N/Yb_N
0
0.5
1
1.5
2
2.5
3
3.5
0
5
10
15
20
25
30

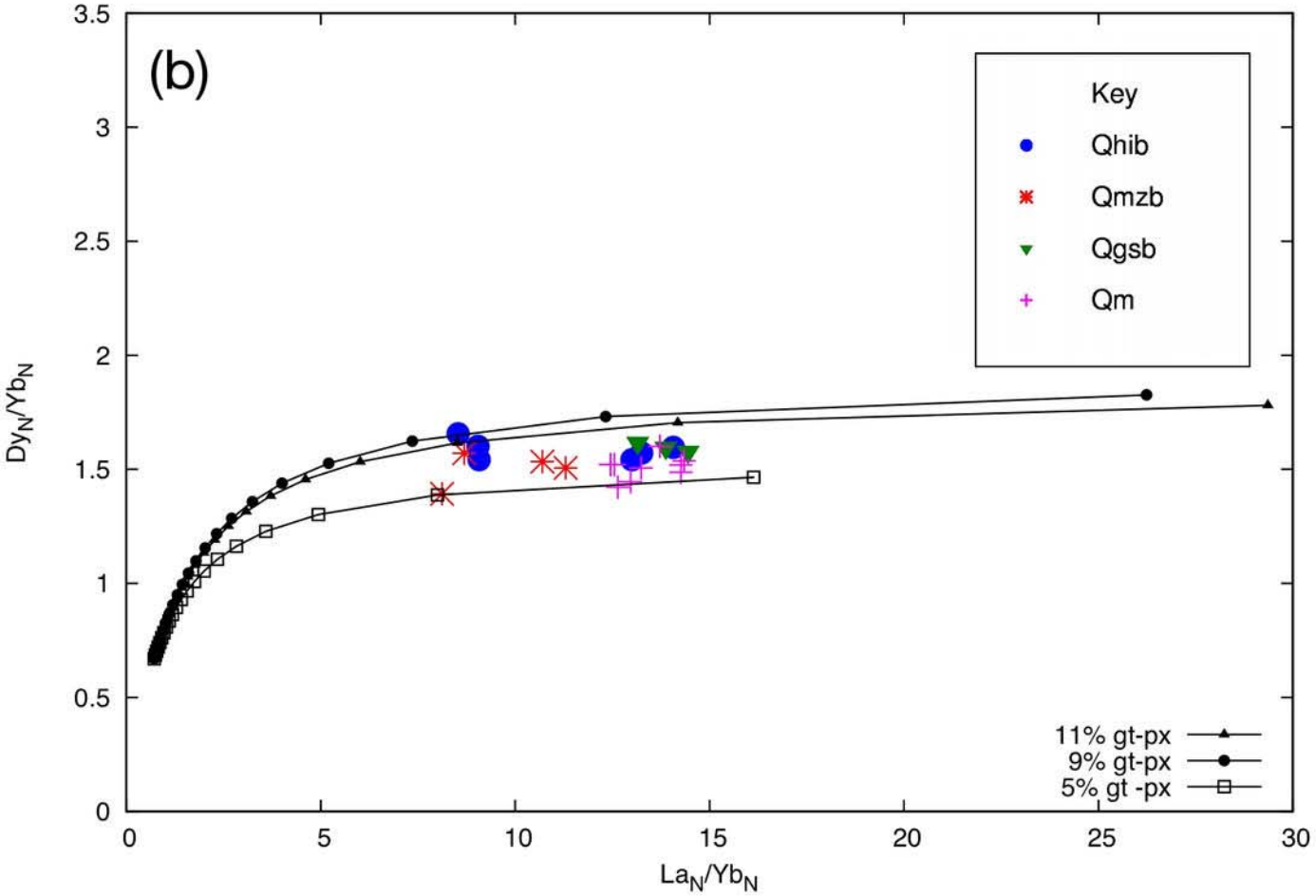
(b)
Key
Qhib
Qmzb
Qgsb
Qm
11% gt-px
9% gt-px
5% gt -px
Dy_N/Yb_N
La_N/Yb_N
0
0.5
1
1.5
2
2.5
3
3.5
0
5
10
15
20
25
30

Table 1. Samples and sample locations.

Sample Number	Latitude	Longitude	Unit	Petrographic description/name
LC10-01	38.5378	-115.9557	Qgsb	Trachybasalt
LC10-02	38.5381	-115.9578	Qmzb	Porphiritic basalt of olivine and plagioclase
LC10-03	38.5391	-115.9565	Qmzb	Porphiritic basalt of olivine and plagioclase
LC10-04	38.5419	-115.9671	Qgsb	Basalt of olivine
LC10-05	38.5449	-115.9713	Qmzb	Trachybasalt
LC10-06	38.5491	-115.9747	Qhib	Basalt of olivine
LC10-07	38.5522	-115.9934	Qhib	Porphiritic basalt of olivine
LC10-08	38.5481	-115.9560	Qhib	Porphiritic basalt of olivine
LC10-09	38.5338	-115.9469	Qgsb	Basalt of olivine (oxidised)
LC10-10	38.5394	-115.9466	Qhib	Basalt of olivine and clinopyroxene
LC10-11	38.5343	-115.9587	Qhib	Trachybasalt
LC10-12	38.5328	-115.9540	Qhib	Porphiritic basalt of plagioclase
LC10-13	38.5394	-115.9509	Qmzb	Porphiritic basalt of plagioclase
LC10-16	38.4823	-115.9777	Qm	Aphanitic basalt
LC10-18	38.4810	-115.9878	Qm	Basalt of olivine
LC10-19	38.4865	-115.9768	Qm	Basalt of olivine and clinopyroxene
LC10-20	38.4886	-115.9852	Qm	Porphiritic basalt of clinopyroxene
LC10-23	38.4908	-116.0046	Qm	Trachybasalt
LC10-24	38.4998	-116.0046	Qm	Basalt of olivine and clinopyroxene
LC10-25	38.4822	-116.0149	Qm	Basalt of olivine
LC10-26a	38.4869	-115.9530	Qm	Aphanitic basalt
LC10-26b	38.4869	-115.9530	Qm	Aphanitic basalt
LC10-26c	38.4869	-115.9530	Qm	Aphanitic basalt
LC10-27	38.4929	-115.9604	Qm	Aphanitic basalt
JCLC11-3	38.4981	-115.9809	Qm	mafic enclave with Amphibole and Olivine Phenocrysts
JCLC11-4a	38.4982	-115.9889	Qm	mafic enclave with Amphibole and Olivine Phenocrysts
JCLC11-4f	38.4982	-115.9889	Qm	mafic enclave with Amphibole and Olivine Phenocrysts

Table 1.- Sample list with location and brief petrographic description

Sample ID	LC10-01	LC10-02	LC10-03	LC10-04	LC10-05	LC10-06	LC10-07	LC10-08	LC10-09	LC10-10	LC10-11	LC10-12	LC10-13	LC10-16	LC10-18	LC10-19	LC10-20	LC10-23	LC10-24	LC10-25	LC10-26a
Unit	Qgsb	Qmzb	Qmzb	Qgsb	Qmzb	Qhib	Qhib	Qhib	Qgsb	Qhib	Qhib	Qhib	Qmzb	Qm	Qm	Qm	Qm	Qm	Qm	Qm	Qm
SiO_2	44.57	47.41	47.33	43.52	45.09	43.39	44.32	45.87	45.02	46.91	45.03	46.40	44.06	45.14	44.34	45.46	44.02	44.56	43.97	44.97	44.54
TiO_2	2.53	2.40	2.30	2.46	2.74	2.51	2.26	2.53	2.29	2.62	2.35	2.48	2.93	2.29	2.28	2.19	2.14	2.33	2.39	2.36	2.13
Al_2O_3	15.12	15.74	15.39	14.34	15.25	14.18	14.03	14.18	14.52	15.71	14.32	15.55	15.20	14.99	14.59	14.82	14.33	15.08	14.88	15.48	13.97
Fe_2O_3	12.75	12.88	12.00	12.87	12.64	12.90	12.29	14.09	11.93	12.32	12.34	13.25	12.57	12.02	11.62	11.00	11.22	11.89	12.59	12.22	11.48
MgO	8.14	7.45	8.32	8.63	8.76	8.48	9.90	10.65	9.69	7.65	9.55	7.44	7.97	9.51	9.44	9.89	10.69	8.23	7.54	7.24	9.98
Na_2O	4.10	4.12	3.65	3.88	3.56	4.31	3.70	3.14	3.63	3.59	3.90	3.80	3.90	3.47	3.89	3.69	3.49	4.14	4.48	4.66	3.88
K_2O	2.09	1.21	1.42	1.90	1.57	1.85	1.77	0.94	1.52	1.41	1.80	1.17	1.83	1.84	1.59	1.78	1.64	1.95	2.02	2.19	1.70
MnO	0.225	0.202	0.180	0.221	0.188	0.227	0.208	0.182	0.208	0.180	0.213	0.195	0.194	0.201	0.212	0.195	0.196	0.223	0.226	0.224	0.203
CaO	10.00	8.78	9.00	10.74	10.16	10.54	10.15	8.71	10.60	9.19	10.52	8.98	9.97	10.56	10.41	10.28	10.57	9.98	9.82	9.60	10.62
P_2O_5	0.969	0.632	0.540	0.867	0.599	0.982	0.688	0.455	0.738	0.556	0.803	0.633	0.596	0.699	0.700	0.632	0.601	0.885	0.902	0.856	0.642
Total	100.50	100.83	100.13	99.43	100.56	99.37	99.32	100.75	100.15	100.14	100.83	99.90	99.22	100.72	99.07	99.94	98.90	99.27	98.82	99.80	99.14
V	186	175	204	197	230	186	199	186	197	185	175	154	225	209	202	208	215	177	178	171	n.d.
Cr	310	130	210	420	200	400	430	220	560	150	450	110	120	400	350	420	460	250	240	210	n.d.
Co	258	275	264	270	266	297	307	320	289	264	224	273	223	308	288	364	337	243	300	247	n.d.
Ni	140	130	130	160	120	170	210	260	210	130	180	120	110	230	170	330	320	140	120	110	n.d.
Cu	50	40	30	50	40	50	50	50	50	30	40	40	30	70	50	120	90	50	40	40	n.d.
Zn	110	130	< 30	110	110	100	100	110	100	110	90	120	100	100	< 30	90	100	< 30	100	100	n.d.
Ga	19	21	19	19	19	16	16	17	17	19	16	20	19	18	17	17	18	18	18	18	n.d.
Ge	2	2	2	2	2	2	2	2	2	2	1	1	2	2	1	2	2	2	2	2	n.d.
As	< 5	< 5	< 5	< 5	< 5	< 5	< 5	< 5	< 5	< 5	< 5	< 5	< 5	< 5	< 5	< 5	< 5	< 5	< 5	< 5	n.d.
Rb	52	21	30	47	31	41	42	15	42	26	39	18	39	44	41	44	40	47	52	52	n.d.
Sr	1090	598	553	973	808	950	760	548	780	635	742	616	718	799	839	790	723	1030	1050	1050	n.d.
Y	32	31	27	30	27	31	28	23	29	27	27	28	27	27	27	27	25	30	31	31	n.d.
Zr	291	198	96	267	215	259	241	143	240	208	225	198	251	245	84	246	225	183	293	300	n.d.
Nb	89	44	30	83	55	80	70	34	71	43	65	42	59	71	49	68	63	71	90	89	n.d.
Mo	3	2	3	4	< 2	4	3	< 2	3	< 2	3	2	3	3	3	3	3	4	4	3	n.d.
Ag	0.6	< 0.5	< 0.5	< 0.5	< 0.5	0.5	< 0.5	< 0.5	< 0.5	< 0.5	< 0.5	< 0.5	0.5	< 0.5	< 0.5	0.5	< 0.5	< 0.5	0.5	0.6	n.d.
In	< 0.2	< 0.2	< 0.2	< 0.2	< 0.2	< 0.2	< 0.2	< 0.2	< 0.2	< 0.2	< 0.2	< 0.2	< 0.2	< 0.2	< 0.2	< 0.2	< 0.2	< 0.2	< 0.2	< 0.2	n.d.
Sn	2	2	2	2	2	2	2	1	2	2	2	2	2	2	1	2	2	2	2	2	n.d.
Sb	< 0.5	< 0.5	< 0.5	< 0.5	< 0.5	< 0.5	< 0.5	< 0.5	< 0.5	< 0.5	< 0.5	< 0.5	< 0.5	< 0.5	< 0.5	< 0.5	< 0.5	< 0.5	< 0.5	< 0.5	n.d.
Cs	< 0.5	< 0.5	< 0.5	< 0.5	< 0.5	0.5	0.6	< 0.5	0.5	< 0.5	< 0.5	< 0.5	< 0.5	0.6	< 0.5	0.5	0.5	0.6	0.7	0.6	n.d.
Ba	665	484	349	602	497	638	545	319	561	441	534	338	507	548	562	538	500	652	728	746	n.d.
La	56.4	31.5	28.3	50.3	35.8	51	42.5	22.6	44	29.1	41.7	29	37.8	44.3	44	42.3	38.2	51.7	54	53.7	n.d.
Ce	114	65.7	56.3	103	71.6	104	84.8	46.9	88.9	60	84.2	59.8	73.7	87	85.7	83	76.1	102	107	105	n.d.
Pr	13.7	8.11	6.69	12.4	8.51	12.8	10.3	5.9	11	7.52	10.5	7.53	8.97	10.5	10.5	10	9.41	12.5	13.2	12.5	n.d.
Nd	54.4	33.9	27.2	48.9	34.9	51.1	41.3	25.2	44.3	31.1	41.9	31.3	35.8	41.7	41.4	39.3	37.1	49.3	51.3	49.5	n.d.
Sm	10.3	7.5	6	9.5	7.4	9.9	8.1	5.7	8.8	6.6	8	6.8	7.4	8	8.1	7.7	7.3	9.2	9.7	9.3	n.d.
Eu	3.06	2.44	1.93	2.82	2.31	2.93	2.45	1.91	2.6	2.21	2.47	2.26	2.35	2.47	2.44	2.35	2.2	2.8	2.93	2.85	n.d.
Gd	8.5	6.9	5.6	7.8	6.4	8	6.9	5.5	7.3	6.3	6.8	6.5	6.5	6.7	6.9	6.6	6.1	7.7	7.9	7.6	n.d.
Tb	1.2	1.1	0.9	1.1	1	1.2	1	0.8	1.1	1	1	1	1	1	1	0.9	0.9	1.1	1.1	1.1	n.d.
Dy	6.6	6.1	5.2	6.2	5.5	6.2	5.4	4.7	5.8	5.3	5.3	5.5	5.4	5.4	5.5	5.1	5	5.9	6.2	6	n.d.
Ho	1.2	1.1	1	1.1	1	1.1	1	0.9	1	1	1	1	1	1	1	1	0.9	1.1	1.1	1.1	n.d.
Er	3.2	3	2.6	3	2.7	3.1	2.7	2.3	2.9	2.7	2.7	2.7	2.7	2.7	2.7	2.7	2.5	3	3.1	3	n.d.
Tm	0.44	0.41	0.38	0.41	0.38	0.42	0.37	0.31	0.39	0.37	0.36	0.37	0.37	0.37	0.38	0.38	0.36	0.41	0.43	0.42	n.d.
Yb	2.8	2.6	2.5	2.6	2.4	2.6	2.3	1.9	2.4	2.3	2.3	2.3	2.4	2.4	2.3	2.4	2.2	2.6	2.7	2.7	n.d.
Lu	0.43	0.41	0.37	0.39	0.36	0.42	0.35	0.29	0.39	0.36	0.36	0.36	0.37	0.38	0.36	0.37	0.34	0.4	0.42	0.41	n.d.
Hf	5.5	4.1	2.1	5.1	4.3	5.2	4.6	3	4.7	4.2	4.4	4	5	4.9	1.5	4.8	4.4	3.4	5.4	5.6	n.d.
Ta	5.2	2.5	2.3	4.7	3.3	5.3	4.6	2.3	4.8	3	4.5	2.8	4.2	5	4.2	4.8	4.4	5.4	6	6	n.d.
W	609	647	557	644	631	738	762	744	701	606	536	618	490	805	635	951	862	576	778	611	n.d.
Tl	< 0.1	< 0.1	< 0.1	< 0.1	< 0.1	< 0.1	< 0.1	< 0.1	< 0.1	< 0.1	< 0.1	< 0.1	< 0.1	< 0.1	< 0.1	< 0.1	< 0.1	< 0.1	< 0.1	< 0.1	n.d.
Pb	< 5	< 5	< 5	< 5	< 5	< 5	< 5	< 5	< 5	< 5	< 5	< 5	< 5	5	< 5	< 5	< 5	< 5	< 5	< 5	n.d.
Bi	< 0.4	< 0.4	< 0.4	< 0.4	< 0.4	< 0.4	< 0.4	< 0.4	< 0.4	< 0.4	< 0.4	< 0.4	< 0.4	< 0.4	< 0.4	< 0.4	< 0.4	< 0.4	< 0.4	< 0.4	n.d.
Th	6.5	2.9	2.9	5.6	4.1	5.3	4.8	1.9	4.8	3	4.5	2.8	4.7	5.7	3.6	5.6	5.1	4.9	6.5	6.7	n.d.
U	1.9	0.8	1	1.7	1.3	1.5	1.3	0.5	1.4	0.8	1.3	0.9	1.4	1.6	1.5	1.6	1.5	1.7	1.8	1.9	n.d.

Table 2. Whole-Rock major and trace element data for samples used in this work. * pyroxenite analysis from GERMS database; n.d. not determined; n.a. not available

LC10-26b Qm	LC10-26c Qm	LC10-27 Qm	pyroxenite*
44.68	44.78	45.82	46.27
1.96	2.12	2.16	1.47
13.85	14.34	13.74	7.16
11.34	11.84	10.89	11.02
10.17	9.19	10.71	16.04
4.06	3.85	3.81	0.92
1.70	1.80	1.67	0.64
0.201	0.210	0.187	0.16
10.12	10.46	10.94	14.08
0.652	0.728	0.714	0.38
98.73	99.32	100.64	98.14
n.d.	190	200	n.a.
n.d.	440	820	n.a.
n.d.	445	390	n.a.
n.d.	170	240	n.a.
n.d.	50	50	n.a.
n.d.	100	80	n.a.
n.d.	17	16	n.a.
n.d.	2	2	n.a.
n.d.	< 5	< 5	n.a.
n.d.	43	37	n.a.
n.d.	848	808	n.a.
n.d.	27	25	n.a.
n.d.	245	178	n.a.
n.d.	74	60	n.a.
n.d.	3	3	n.a.
n.d.	< 0.5	< 0.5	n.a.
n.d.	< 0.2	< 0.2	n.a.
n.d.	2	2	n.a.
n.d.	< 0.5	< 0.5	n.a.
n.d.	0.5	< 0.5	n.a.
n.d.	572	550	n.a.
n.d.	45.2	38.5	n.a.
n.d.	89.2	77	n.a.
n.d.	10.9	9.51	n.a.
n.d.	42.5	37.9	n.a.
n.d.	8.2	7.5	n.a.
n.d.	2.52	2.33	n.a.
n.d.	6.8	6.4	n.a.
n.d.	1	0.9	n.a.
n.d.	5.4	5	n.a.
n.d.	1	0.9	n.a.
n.d.	2.7	2.5	n.a.
n.d.	0.38	0.35	n.a.
n.d.	2.5	2.2	n.a.
n.d.	0.38	0.34	n.a.
n.d.	4.8	3.4	n.a.
n.d.	5	4.3	n.a.
n.d.	1200	1010	n.a.
n.d.	< 0.1	< 0.1	n.a.
n.d.	< 5	< 5	n.a.
n.d.	< 0.4	< 0.4	n.a.
n.d.	5.4	4.5	n.a.
n.d.	1.6	1.4	n.a.

Sample	LC10-06	LC10-06	LC10-03	LC10-03	LC10-01	LC10-23	LC10-20	LC10-26A
unit	Qhib	Qhib	Qmzb	Qmzb	Qgsb	Qm	Qm	Qm
SiO_2	38.77	40.28	37.66	40.25	40.39	37.28	39.32	40.03
TiO_2	0.14	0.00	0.05	0.01	0.01	0.09	0.04	0.00
Al_2O_3	0.68	0.05	0.01	0.04	0.08	0.06	0.04	0.06
Cr_2O_3	0.02	0.07	0.00	0.01	0.03	0.19	0.03	0.02
FeO	22.06	11.40	32.15	17.48	12.05	28.25	17.47	12.10
MnO	0.47	0.17	0.83	0.24	0.16	0.62	0.33	0.19
MgO	39.31	48.42	30.37	43.12	48.21	34.34	43.35	47.36
NiO	0.12	0.00	0.03	0.17	0.00	0.04	0.20	0.00
CaO	0.43	0.29	0.42	0.22	0.27	0.63	0.40	0.29
Total	101.99	100.67	101.51	101.54	101.21	101.51	101.19	100.06
Si	0.98	0.99	1.01	1.01	0.99	0.99	0.99	0.99
Ti	0.00	0.00	0.00	0.00	0.00	0.00	0.00	0.00
Al	0.02	0.00	0.00	0.00	0.00	0.00	0.00	0.00
Cr	0.00	0.00	0.00	0.00	0.00	0.00	0.00	0.00
Fe^{2+}	0.47	0.23	0.72	0.37	0.25	0.62	0.37	0.25
Mn	0.01	0.00	0.02	0.01	0.00	0.01	0.01	0.00
Mg	1.49	1.77	1.22	1.61	1.76	1.35	1.63	1.75
Ni	0.00	0.00	0.00	0.00	0.00	0.00	0.00	0.00
Ca	0.01	0.01	0.01	0.01	0.01	0.02	0.01	0.01
Total	2.99	3.01	2.99	2.99	3.01	3.00	3.01	3.00
%Fo	75.66	88.18	62.14	81.27	87.56	67.95	81.27	87.29

Table 3a.-Representative EPMA analysis of olivine phenocrysts in wt% and in cation per formula unit, recalculated to 4 oxygens. %Fo=Mg/(Mg+Fe+Mn)

Sample	LC10-12	LC10-06	LC10-12	LC10-03	LC10-03	LC10-01	LC10-01	LC10-23	LC10-20
unit	Qhib	Qhib	Qhib	Qmzb	Qmzb	Qgsb	Qgsb	Qm	Qm
SiO_2	43.05	46.92	50.07	49.84	49.47	44.61	50.51	44.38	49.55
TiO_2	4.00	2.45	0.65	0.60	0.00	3.51	0.53	3.37	0.81
Al_2O_3	9.42	6.85	7.67	5.17	5.01	8.42	7.50	8.05	7.28
Cr_2O_3	0.06	0.19	0.68	0.00	0.00	0.06	0.88	0.00	0.47
FeO	9.46	7.88	4.64	9.81	9.94	8.73	4.75	10.02	4.47
MnO	0.18	0.15	0.10	0.21	0.24	0.20	0.08	0.20	0.10
MgO	10.24	12.52	16.43	12.76	13.42	10.87	16.79	11.22	15.51
NiO	0.00	0.02	0.00	0.00	0.00	0.02	0.04	0.00	0.01
CaO	22.76	22.82	19.61	19.37	20.01	23.66	18.69	22.61	21.35
Na_2O	0.57	0.44	0.86	1.53	1.45	0.55	0.72	0.50	0.52
K_2O	0.05	0.08	0.01	0.00	0.02	0.03	0.00	0.03	0.01
P_2O_5	0.17	0.11	0.01	0.00	0.00	0.26	0.00	0.21	0.02
Total	99.97	100.45	100.78	99.29	99.57	100.91	100.49	100.60	100.10
Si	1.64	1.75	1.81	1.88	1.86	1.68	1.83	1.68	1.81
Ti	0.11	0.07	0.02	0.02	0.00	0.10	0.01	0.10	0.02
Al	0.42	0.30	0.33	0.23	0.22	0.37	0.32	0.36	0.31
Cr	0.00	0.01	0.02	0.00	0.00	0.00	0.03	0.00	0.01
Fe^{3+}	0.11	0.08	0.06	0.09	0.15	0.11	0.02	0.13	0.04
Fe^{2+}	0.19	0.17	0.09	0.21	0.16	0.16	0.12	0.19	0.09
Mn	0.01	0.00	0.00	0.01	0.01	0.01	0.00	0.01	0.00
Mg	0.58	0.70	0.89	0.72	0.75	0.61	0.90	0.63	0.85
Ni	0.00	0.00	0.00	0.00	0.00	0.00	0.00	0.00	0.00
Ca	0.93	0.91	0.76	0.78	0.81	0.95	0.72	0.92	0.84
Na	0.04	0.03	0.06	0.11	0.11	0.04	0.05	0.04	0.04
K	0.00	0.00	0.00	0.00	0.00	0.00	0.00	0.00	0.00
P	0.01	0.00	0.00	0.00	0.00	0.01	0.00	0.01	0.00
Total	4.05	4.04	4.03	4.05	4.08	4.04	4.01	4.05	4.02
Mg#	0.75	0.80	0.91	0.76	0.82	0.78	0.88	0.76	0.90

Table 3b.- Representative EPMA analysis of clinopyroxene phenocrysts in wt% and in cation per formula unit recalculated to 6 oxygens. Speciation of iron was calculated following Papike (1974).

Comment	LC10-12	LC10-06	LC10-06	LC10-03	LC10-03	LC10-01	LC10-01	LC10-26A	LC10-26A	LC10-20
unit	Qhib	Qhib	Qhib	Qmzb	Qmzb	Qgsb	Qgsb	Qm	Qm	Qm
SiO_2	55.32	49.84	50.12	57.26	50.60	52.14	50.35	61.29	50.15	49.44
TiO_2	0.08	0.31	0.11	0.03	0.10	0.17	0.14	0.04	0.29	0.12
Al_2O_3	28.25	29.54	31.48	25.45	31.27	30.49	31.56	25.02	30.87	31.86
Cr_2O_3	0.01	0.00	0.01	0.02	0.00	0.00	0.10	0.01	0.00	0.04
Fe_2O_3	0.24	1.74	0.74	0.40	0.56	0.92	0.76	0.35	1.30	0.67
SrO	0.02	0.01	0.00	0.00	0.00	0.00	0.00	0.00	0.00	0.00
MnO	0.01	0.03	0.02	0.01	0.01	0.00	0.00	0.00	0.01	0.01
MgO	0.01	0.54	0.11	0.02	0.09	0.07	0.05	0.00	0.23	0.09
CaO	10.09	13.93	14.64	6.94	14.07	12.46	14.24	5.91	14.32	14.79
Na_2O	5.57	3.46	3.07	7.58	3.37	4.31	3.24	6.47	3.39	2.88
K_2O	0.44	0.43	0.30	0.90	0.26	0.61	0.29	0.88	0.41	0.28
Total	100.04	99.83	100.60	98.61	100.33	101.17	100.72	99.95	100.99	100.18
Si	2.49	2.29	2.28	2.61	2.30	2.35	2.28	2.72	2.28	2.26
Ti	0.00	0.01	0.00	0.00	0.00	0.01	0.00	0.00	0.01	0.00
Al	1.50	1.60	1.69	1.37	1.68	1.62	1.69	1.31	1.65	1.71
Cr	0.00	0.00	0.00	0.00	0.00	0.00	0.00	0.00	0.00	0.00
Fe^{3+}	0.01	0.06	0.03	0.01	0.02	0.03	0.03	0.01	0.04	0.02
Sr	0.00	0.00	0.00	0.00	0.00	0.00	0.00	0.00	0.00	0.00
Mn	0.00	0.00	0.00	0.00	0.00	0.00	0.00	0.00	0.00	0.00
Mg	0.00	0.04	0.01	0.00	0.01	0.00	0.00	0.00	0.02	0.01
Ca	0.49	0.69	0.71	0.34	0.69	0.60	0.69	0.28	0.70	0.72
Na	0.49	0.31	0.27	0.67	0.30	0.38	0.29	0.56	0.30	0.25
K	0.03	0.03	0.02	0.05	0.02	0.04	0.02	0.05	0.02	0.02
Total	5.01	5.03	5.00	5.06	5.00	5.02	5.00	4.92	5.02	5.00
%An	48.76	67.27	71.21	31.92	68.69	59.34	69.63	31.67	68.35	72.76

Table 3c.- Representative EPMA analyses of plagioclase phenocrysts in wt% and in cation per formula unit, recalculated to 8 oxygens. %An=Ca/(Ca+Na

Sample	JCLC11-4a	JCLC11-4a	JCLC11-4c	JCLC11-4c	JCLC11-4f	JCLC11-4c	JCLC11-4c	JCLC11-4c	JCLC11-4f	JCLC11-4f	JCLC11-4f
	core	core	core	core	clusion in olivi	rim	rim	rim	core	core	core
Unit	Qm	Qm	Qm	Qm	Qm	Qm	Qm	Qm	Qm	Qm	Qm
SiO_2	41.83	41.85	41.07	41.59	40.69	41.94	41.55	42.06	40.51	40.62	40.37
TiO_2	4.27	4.36	4.38	3.27	4.97	3.00	3.58	2.74	5.19	5.19	5.62
$A_{l2}O_3$	15.08	15.07	14.78	15.11	15.17	14.74	14.32	14.66	15.10	15.41	15.58
FeO	9.18	9.18	10.76	11.02	10.06	11.00	10.74	10.91	9.64	9.74	9.86
MnO	0.11	0.11	0.14	0.14	0.11	0.10	0.13	0.08	0.11	0.10	0.11
MgO	14.02	14.01	13.55	13.47	13.76	13.58	13.99	14.07	13.68	14.02	13.20
CaO	11.81	11.67	11.37	11.41	11.43	11.44	11.49	11.53	11.61	11.63	11.79
Na_2O	3.05	3.15	2.93	3.05	2.73	2.76	2.81	2.56	2.79	2.89	2.88
K_2O	0.50	0.47	0.97	0.89	1.14	1.29	1.18	1.40	1.18	1.06	1.07
Total	99.84	99.85	99.94	99.93	100.06	99.84	99.78	100.01	99.81	100.66	100.48
Si(T)	5.954	5.953	5.887	5.953	5.815	6.013	5.962	6.008	5.814	5.771	5.771
Al(T)	2.046	2.047	2.113	2.047	2.185	1.987	2.038	1.992	2.186	2.229	2.229
Al(C)	0.483	0.479	0.383	0.500	0.370	0.503	0.382	0.476	0.367	0.350	0.395
Ti(C)	0.457	0.466	0.472	0.352	0.534	0.323	0.386	0.294	0.560	0.555	0.604
Cr(C)	0.000	0.000	0.000	0.000	0.000	0.000	0.000	0.000	0.000	0.000	0.000
Fe^{3+}(C)	0.074	0.080	0.193	0.215	0.180	0.205	0.226	0.277	0.088	0.152	0.014
Mg(C)	2.976	2.971	2.895	2.874	2.932	2.902	2.992	2.997	2.927	2.970	2.813
Ni(C)	0.000	0.000	0.000	0.000	0.000	0.000	0.000	0.000	0.000	0.000	0.000
Fe^{2+}(C)	1.004	0.997	1.049	1.050	0.978	1.061	1.006	0.951	1.051	0.967	1.165
Mn(C)	0.006	0.007	0.008	0.008	0.007	0.006	0.008	0.005	0.007	0.006	0.009
Mg(B)	0.000	0.000	0.000	0.000	0.000	0.000	0.000	0.000	0.000	0.000	0.000
Ni(B)	0.000	0.000	0.000	0.000	0.000	0.000	0.000	0.000	0.000	0.000	0.000
Fe^{2+}(B)	0.015	0.016	0.047	0.053	0.044	0.052	0.057	0.075	0.018	0.037	0.000
Mn(B)	0.006	0.007	0.008	0.008	0.007	0.006	0.008	0.005	0.007	0.006	0.004
Ca(B)	1.800	1.779	1.746	1.749	1.751	1.757	1.766	1.765	1.785	1.770	1.806
Na(B)	0.179	0.198	0.199	0.190	0.198	0.185	0.169	0.156	0.190	0.186	0.190
Na(A)	0.663	0.669	0.615	0.655	0.557	0.582	0.611	0.551	0.585	0.611	0.608
K(A)	0.091	0.084	0.178	0.162	0.208	0.235	0.216	0.255	0.216	0.193	0.195
T	8	8	8	8	8	8	8	8	8	8	8
C	4.53	5	5	5	4.58	5	5	5	5	4.58	4.42
B	2	2	2	2	2	2	2	2	2	2	2
A	0.75	0.75	0.79	0.82	0.77	0.82	0.83	0.81	0.80	0.80	0.80
H_2O amp (wt.%	1.97	1.97	1.97	1.96	1.96	1.97	1.97	1.99	1.99	1.98	1.98
H_2O melt (wt.%	5.95	6.76	5.71	5.92	5.33	5.57	5.56	5.70	7.41	6.16	7.44
P (MPa)	685.36	736.41	746.48	678.87	613.45	654.11	749.79	774.48	721.77	834.85	725.37
T (°C)	1037.14	1028.52	1052.92	1017.28	1023.94	1015.80	1059.59	1064.95	1040.15	1070.75	1041.14
ΔNNO	-0.10	0.10	-0.16	0.24	0.26	0.51	-0.31	-0.21	-0.12	-0.64	-0.09

Table 3d.- Representative EPMA analyses of Amphiboles, found in mafic inclusions in Marcath products, in wt% and recalculated to 23 oxygens, (average of maximum and minimum estimation of ferric iron), following Leake et al., (1997).
Calculations of water, temperature pressure and oxygen fugacity has been done following Ridolfi et al., (2012).

	Cr	Th	Ta	Dy	La	Yb
Olivine	0.7	0.03	0.03	0.013	0.0067	0.03
Clinopyroxene	34	0.03	0.013	0.582	0.056	0.542
Orthopyroxene	10	0.04	0.0008	0.15	0.03	0.34
Garnet	2.9	0.044	0.06	3.17	0.001	11.5
Spinel	3.43	0.01	0.0004	0.01	0.01	0.01

Table 4a. Partition coefficients used in this study.
Data from Rollinson, (1993) and from the Earth Reference Database (http://earthref.org).

	D Cr	D Th	D Ta	D Dy	D La	D Yb
px1	13.6563	0.03424	0.019436	0.57067	0.027653	1.535
px2	13.6053	0.03366	0.018536	0.5074	0.0277	1.3053
px3	13.6983	0.03604	0.021236	0.57145	0.028055	1.5368
lz1	5.488	0.03368	0.0264	0.46476	0.01462	1.50936
lz2	7.185	0.0329	0.022866	0.27496	0.01795	0.73826
lz3	7.2889	0.0321	0.019188	0.11818	0.019006	0.17454
lz4	8.877	0.03258	0.020824	0.21007	0.020819	0.42286

Table 4b. Calculated bulk partition coefficients using the modal mineralogies below

px1 =29%ol+29%opx+30%cpx+11%gt+1%sp
px2 =30%ol+40%opx+20%cpx+9%gt+1%sp
px3 =35%ol+29%opx+30%cpx+5%gt+1%sp
lz1 =60%ol+20%opx+8%cpx+12%gt
lz2 =60%ol+22%opx+13%cpx+5%gt
lz3 =58%ol+27%opx+12%cpx+3%sp
lz3 =57%ol+23%opx+18%cpx+2%gt

Pressure (Gpa)	model	sample	Liquidus (C)
0.3	MELTS	LC10-20	1276
0.6	MELTS	LC10-20	1296
0.9	pMELTS	LC10-20	1279
1	pMELTS	LC10-20	1284
1.3	pMELTS	LC10-20	1318
1.7	pMELTS	LC10-20	1370
3	pMELTS	LC10-20	1584
3	pMELTS	pyroxenite*	1581
3.8	pMELTS	LC10-20	1673
3.8	pMELTS	pyroxenite*	1664

Table 5.- Summary of MELTS and pMELTS calculated liquidus temperatures in samples (see text for deta

* pyroxenite from GERMS database